

3-21-2018

# Dynamics of human protein kinases linked to drug selectivity


Dorothee Kern  
*Brandeis University*

Warintra Pitsawong  
*Brandeis University*

Brandeis University

*See next page for additional authors*

Follow this and additional works at: [https://escholarship.umassmed.edu/faculty\\_pubs](https://escholarship.umassmed.edu/faculty_pubs)

 Part of the [Amino Acids, Peptides, and Proteins Commons](#), [Biochemistry Commons](#), [Biophysics Commons](#), [Enzymes and Coenzymes Commons](#), and the [Structural Biology Commons](#)

---

## Repository Citation

Kern, Dorothee; Pitsawong, Warintra; Brandeis University; Otten, Renee; Agafonov, Roman V.; Zorba, Adelajda; Kern, Nadja; Kutter, Steffen; Kern, Gunther; Pádua, Ricardo A.P.; and Meniche, Xavier, "Dynamics of human protein kinases linked to drug selectivity" (2018). *University of Massachusetts Medical School Faculty Publications*. 1536.  
[https://escholarship.umassmed.edu/faculty\\_pubs/1536](https://escholarship.umassmed.edu/faculty_pubs/1536)

---

# Dynamics of human protein kinases linked to drug selectivity

## Authors

Dorothee Kern, Warintra Pitsawong, Brandeis University, Renee Otten, Roman V. Agafonov, Adelajda Zorba, Nadja Kern, Steffen Kutter, Gunther Kern, Ricardo A.P. Pádua, and Xavier Meniche

## Keywords

protein kinases, drugs, binding, Ser/Thr-kinase Aurora A

## Creative Commons License



This work is licensed under a [Creative Commons Attribution 4.0 License](https://creativecommons.org/licenses/by/4.0/).

## Rights and Permissions

The copyright holder for this preprint (which was not peer-reviewed) is the author/funder. It is made available under a [CC-BY 4.0 International license](https://creativecommons.org/licenses/by/4.0/).

## 1                    **Dynamics of human protein kinases linked to drug selectivity**

2  
3  
4    Warintra Pitsawong<sup>\*,a</sup>, Vanessa Buosi<sup>\*,a</sup>, Renee Otten<sup>\*,a</sup>, Roman V. Agafonov<sup>\*,a</sup> Adelajda Zorba<sup>a</sup>,  
5    Nadja Kern<sup>a</sup>, Steffen Kutter<sup>a</sup>, Gunther Kern<sup>a</sup>, Ricardo A. P. Pádua<sup>a</sup>, Xavier Meniche<sup>b</sup>, and  
6    Dorothee Kern<sup>#,a</sup>

7  
8    <sup>a</sup>*Department of Biochemistry and Howard Hughes Medical Institute, Brandeis University,*  
9    *Waltham, MA 02452, USA*

10    <sup>b</sup>*Department of Microbiology and Physiological Systems, University of Massachusetts Medical*  
11    *School, Worcester, MA 01605, USA*

12    \*these authors contributed equally to this work

13    #corresponding author

### 14 15    **Abstract**

16    Protein kinases are major drug targets, but the development of highly-selective inhibitors has  
17    been challenging due to the similarity of their active sites. The observation of distinct structural  
18    states of the fully-conserved Asp-Phe-Gly (DFG) loop has put the concept of conformational  
19    selection for the DFG-state at the center of kinase drug discovery. Recently, it was shown that  
20    Gleevec selectivity for the Tyr-kinases Abl was instead rooted in conformational changes after  
21    drug binding. Here, we investigate whether protein dynamics after binding is a more general  
22    paradigm for drug selectivity by characterizing the binding of several approved drugs to the  
23    Ser/Thr-kinase Aurora A. Using a combination of biophysical techniques, we propose a universal  
24    drug-binding mechanism, that rationalizes selectivity, affinity and long on-target residence time  
25    for kinase inhibitors. These new concepts, where protein dynamics in the drug-bound state plays  
26    the crucial role, can be applied to inhibitor design of targets outside the kinome.

### 27 28    **eLife digest**

29    The Ser/Thr kinase Aurora A is an important target for the development of new anticancer  
30    therapies. A longstanding question is how to specifically and effectively inhibit only this kinase in  
31    a background of over 550 protein kinases with very similar structures. To this end, understanding  
32    the inhibition mechanism of Aurora A by different drugs is essential. Here, we characterize the  
33    kinetic mechanism of three distinct kinase drugs, Gleevec (Imatinib), Danusertib (PHA739358)  
34    and AT9283 (Pyrazol-4-yl Urea) for Aurora A. We show that inhibitor affinities do not rely  
35    exclusively on the recognition of a specific conformation of the Asp-Phe-Gly loop of the kinase.

36 Our quantitative kinetics data put forward an opposing mechanism in which a slow conformational  
37 change after drug binding (i.e., induced-fit step) dictates drug affinity.

38

## 39 **Introduction**

40 Protein kinases have become the number one drug target of the 21<sup>th</sup> century (Cohen, 2002;  
41 Hopkins & Groom, 2002), due to their central role in cellular processes and involvement in various  
42 types of cancer (Carvajal, Tse, & Schwartz, 2006; Gautschi et al., 2008; Katayama & Sen, 2010).  
43 Despite their therapeutic significance, the development of specific kinase inhibitors proves to be  
44 extremely challenging because they must discriminate between the very similar active sites of a  
45 large number of kinases in human cells. One of the biggest success stories is Gleevec: a highly  
46 selective drug that specifically targets Abl kinase, providing an efficient treatment of chronic  
47 myelogenous leukemia (CML) and minimizing side effects (Iqbal & Iqbal, 2014). Despite being a  
48 multi-billion-dollar cancer drug, the mechanism responsible for its impressive selectivity has been  
49 elusive until recently. It has long been proposed that the conformational state of the fully  
50 conserved DFG (for Asp-Phe-Gly) loop (Taylor, Keshwani, Steichen, & Kornev, 2012) dictates the  
51 selectivity for Gleevec and other kinase inhibitors (Lovera et al., 2012; Treiber & Shah, 2013).  
52 Recent quantitative binding kinetics put forward an opposing mechanism in which an induced-fit  
53 step after drug binding is responsible for Gleevec's selectivity (Agafonov, Wilson, Otten, Buosi, &  
54 Kern, 2014; Wilson et al., 2015).

55 Here we ask the question whether this fundamentally different mechanism is a more  
56 general principle for drug efficacy and selectivity not only for Tyr kinases such as Abl, but also for  
57 Ser/Thr kinases. To this end, we chose the Ser/Thr kinase Aurora A and investigated the binding  
58 kinetics of three distinct kinase drugs: Danusertib, AT9283, and Gleevec. Aurora A kinase is one  
59 of the key regulators of mitotic events, including mitotic entry, centrosome maturation and spindle  
60 formation (Fu, Bian, Jiang, & Zhang, 2007; Lukasiewicz & Lingle, 2009; Marumoto, Zhang, &  
61 Saya, 2005), as well as assisting in neuronal migration (Nikonova, Astsaturov, Serebriiskii,  
62 Dunbrack, & Golemis, 2013). Aurora A has attracted significant attention for the development of  
63 targeted agents for cancer because it is overexpressed in a wide range of tumors, including  
64 breast, colon, ovary and skin malignancies (Carvajal et al., 2006; Gautschi et al., 2008; Katayama  
65 & Sen, 2010; Lok, Klein, & Saif, 2010; Marzo & Naval, 2013). The focus was mainly on ATP-  
66 competitive inhibitors, but more recently inhibition by allosteric compounds has also been pursued  
67 with the aim of achieving higher selectivity (Asteriti et al., 2017; Bayliss, Burgess, & McIntyre,  
68 2017; Burgess et al., 2016; Janecek et al., 2016; McIntyre et al., 2017). So far, only the clinical  
69 significance of Aurora A inhibition by ATP-competitive drugs has been established (Bavetsias &



70 Linardopoulos, 2015; Borisa & Bhatt, 2017), but little is known about their binding mechanisms.  
71 Many high-resolution X-ray structures of Aurora A kinase bound to different inhibitors have been  
72 solved (Bavetsias et al., 2015; Dodson et al., 2010; Fancelli et al., 2006; Ferguson et al., 2017;  
73 Heron et al., 2006; Howard et al., 2009; Kilchmann et al., 2016; Martin et al., 2012; Zhao et al.,  
74 2008), but the selectivity profile of those kinase inhibitors remains very difficult to explain.

75 The drugs used in this study are small, ATP-competitive inhibitors. Danusertib  
76 (PHA739358) and AT9283 were developed for Aurora kinases, whereas Gleevec is selective for  
77 the Tyr kinase Abl. Danusertib inhibits all members of the Aurora family with low nanomolar IC<sub>50</sub>  
78 values (13, 79 and 61 nM for Aurora A, B and C, respectively) (Carpinelli et al., 2007; Fraedrich  
79 et al., 2012) and was one of the first Aurora kinase inhibitors to enter phase I and II clinical trials  
80 (Kollareddy et al., 2012; Steeghs et al., 2009). A crystal structure of Danusertib bound to Aurora  
81 A kinase shows an inactive kinase with the DFG-loop in the *out* conformation (Fancelli et al.,  
82 2006). AT9283 inhibits both Aurora A and B with an IC<sub>50</sub> of 3 nM (Howard et al., 2009) and has  
83 also entered several clinical trials (Borisa & Bhatt, 2017). Interestingly, the crystal structure of  
84 Aurora A with AT9283 shows that this drug binds to the DFG-*in*, active conformation of the kinase  
85 (Howard et al., 2009). Both drugs are high-affinity binders that reportedly bind to a discrete kinase  
86 conformation and would allow us to probe for a conformational-selection step. Lastly, we selected  
87 Gleevec as a drug that is not selective for Aurora A and should, therefore, have a weaker binding  
88 affinity. We reasoned that this choice of inhibitors could reveal general mechanisms underlying  
89 drug selectivity and affinity.

90 The combination of X-ray crystallography, NMR spectroscopy and comprehensive  
91 analysis of drug binding and release kinetics delivered a general mechanistic view. Differential  
92 drug affinity is not rooted in the overwhelmingly favored paradigm of the DFG-conformation, but  
93 instead in the dynamic personality of the kinase that is manifested in conformational changes  
94 after drug binding. Notably, such conformational changes have evolved for its natural substrates,  
95 and the drugs take advantage of this built-in protein dynamics.

96

## 97 **Results**

### 98 **Dephosphorylated Aurora A samples both an inactive and active structure**

99 A plethora of X-ray structures and functional assays led to the general notion that  
100 dephosphorylated Aurora A and, more universally, Ser/Thr kinases are in an inactive  
101 conformation and that phosphorylation or activator binding induces the active structure. A  
102 comparison of many X-ray structures of inactive and active forms of Ser/Thr kinases resulted in  
103 an elegant proposal of the structural hallmarks for the active state by Taylor and collaborators:

104 the completion of both the regulatory and catalytic spines spanning the N- and C-terminal  
105 domains, including the orientation of the DFG-motif (Kornev & Taylor, 2010, 2015).

106 To our surprise, two crystals from the same crystallization well capture both the inactive  
107 and active conformations of dephosphorylated Aurora A bound with AMPPCP (Figure 1A, B). As  
108 anticipated, the first structure (PDB 4C3R (Zorba et al., 2014)) superimposes with the well-known  
109 inactive, dephosphorylated Aurora A structure (PDB 1MUO (Cheetham et al., 2002)) and the  
110 activation loop is not visible as commonly observed for kinases lacking phosphorylation of the  
111 activation loop (Zorba et al., 2014). Unexpectedly, the second structure (PDB 6CPF; Figure 1-  
112 *figure supplement 1*) adopts the same conformation as the previously published phosphorylated,  
113 active structure (PDB 1OL7 (Bayliss, Sardon, Vernos, & Conti, 2003)) (Figure 1C) and the first  
114 part of the activation loop could be built, although the B-factors are high. Every hallmark of an  
115 active state is seen for this dephosphorylated protein, including the DFG-*in* conformation that is  
116 essential for completing the regulatory spine. In contrast, the DFG-loop is in the *out* position for  
117 the inactive form of Aurora A (Figure 1D, cyan). In the active, non-phosphorylated structure,  
118 electron density is seen in the canonical tighter Mg<sup>2+</sup>-binding site, where the metal ion is  
119 coordinated to the  $\alpha$ - and  $\beta$ -phosphates of AMPPCP and Asp274. The presence of the metal is  
120 supported by the CheckMyMetal (Zheng et al., 2017) validation except that the coordination is  
121 incomplete. We surmise that two water molecules, not visible in our data, complete the  
122 coordination sphere as is seen in several higher-resolution structures. In the inactive structure,  
123 no electron density for Mg<sup>2+</sup> can be identified possibly due to the fact that Asp274 is rotated to the  
124 DFG-*out* position and is, therefore, lost as coordination partner. Furthermore, sampling of the  
125 active conformation does not depend on AMPPCP binding as dephosphorylated, apo Aurora A  
126 also crystallizes in the active form (PDB 6CPE; Figure 1E, F and Figure 1-*figure supplement 1*).

127 We note that in Aurora kinase sequences a tryptophan residue, Trp277, is immediately  
128 following the DFG motif and displays a drastically different orientation whether Aurora A is in an  
129 active (DFG-*in*) or inactive (DFG-*out*) conformation (Figure 1D). This Trp moiety is unique for the  
130 Aurora kinase family in the Ser/Thr kinome and its position is suggested to be important for tuning  
131 the substrate specificity (C. Chen et al., 2014). We used this Trp residue as probe to monitor the  
132 DFG flip and drug binding in real time as described below.

133 The fact that the inactive and active states are seen in the crystal implies that both are  
134 sampled; however, it does not deliver information about the relative populations or interconversion  
135 rates. Therefore, we set out to monitor the conformational exchange of the DFG-*in/out* flip in  
136 solution. Owing to the reported importance of the DFG flip for activity, regulation and drug design,  
137 there have been extensive efforts to characterize this conformational equilibrium by computation

138 (Badrinarayan & Sastry, 2014; Barakat et al., 2013; Meng, Lin, & Roux, 2015; Sarvagalla &  
139 Coumar, 2015). As an experimental approach, NMR spectroscopy is an obvious choice; however  
140 efforts on several Ser/Thr and Tyr kinases led to the general conclusion that the activation loop,  
141 including the DFG motif and most of the active-site residues, cannot be detected due to exchange  
142 broadening, and at best can only be seen after binding of drugs that stabilize conformations  
143 (Campos-Olivas, Marenchino, Scapozza, & Gervasio, 2011; Langer et al., 2004; Vajpai et al.,  
144 2008; Vogtherr et al., 2006).

145  $[^1\text{H}-^{15}\text{N}]$ -HSQC experiments on uniformly  $^{15}\text{N}$ -labeled samples of Aurora A proved to be  
146 no exception: many peaks are missing and only three out of four tryptophan side chain indole  
147 signals are seen in the 2D spectra of a  $[^{15}\text{N}]$ -Trp labeled sample (Figure 2A, B). Therefore, we  
148 sought a strategy to overcome this general problem of exchange broadening that hampers the  
149 detection of the DFG equilibrium. Aurora A was produced containing 5-fluoro-tryptophan residues  
150 to allow for one-dimensional  $^{19}\text{F}$  spectroscopy to deal with exchange broadening while providing  
151 sensitivity close to proton NMR (Kitevski-LeBlanc & Prosser, 2012). Now, we observe as expected  
152 four peaks in our NMR spectra for apo- and AMPPCP-bound wild-type Aurora A (Figure 2C). A  
153 deconvolution of the spectrum yields almost identical integral values for all four peaks, whereas  
154 the linewidth of one resonance is approximately 5-fold larger (Figure 2D, purple signal). This  
155 broad peak is a prime candidate to originate from Trp277, directly adjacent to the DFG-loop. The  
156 W277L mutation confirmed our hypothesis (Figure 2C), and the extensive line broadening of this  
157 signal in a one-dimensional spectrum is consistent with its absence in the  $[^1\text{H},^{15}\text{N}]$ -HSQC  
158 spectrum. Of note, the W277L mutant is still active, as confirmed by a kinase assay, most likely  
159 because this Trp is not conserved in Ser/Thr kinases, where a Leu residue is found at the position  
160 for several Ser/Thr family members. Mutating any of the other, more conserved Trp residues  
161 resulted in insoluble proteins. The broad line shape for the Trp277 peak hints at severe exchange  
162 broadening in the surrounding of the DFG-loop and is consistent with the high B-factors for Trp277  
163 and its neighboring residues observed in all crystal structures described here. Determination of  
164 relative populations and rate constants of interconversion is not possible from this data, but this  
165 missing piece of information was obtained by stopped-flow kinetics of drug binding.

166

### 167 **Gleevec binding to Aurora A distinguishes conformational selection versus induced-fit** 168 **mechanisms**

169 Through groundbreaking experiments on the Tyr kinases Abl and Src, the concept of drug  
170 selectivity based on the DFG-loop conformation has received considerable attention in kinase  
171 drug discovery (Lovera et al., 2012; Treiber & Shah, 2013). A recent report provides kinetic

172 evidence for such conformational selection, but identifies an induced-fit step after drug binding as  
173 the overwhelming contribution for Gleevec selectivity towards Abl compared to Src (Agafonov et  
174 al., 2014). Here, we ask the obvious question if this mechanism of Gleevec binding to Abl might  
175 exemplify a more general mechanism for kinase inhibitors.

176 To assess which kinetic steps control drug affinity and selectivity, we first studied the  
177 binding kinetics for Gleevec to Aurora A by stopped-flow spectroscopy using intrinsic tryptophan  
178 fluorescence under degassing conditions to reduce photobleaching. At 25 °C, the binding of  
179 Gleevec to Aurora A was too fast to be monitored and, therefore, experiments were performed at  
180 10 °C. Binding kinetics of Gleevec to Aurora A exhibited biphasic kinetic traces (Figure 3A). The  
181 first, fast phase is characterized by a decrease in the fluorescence intensity (Figure 3A, B), with  
182 an observed rate constant,  $k_{obs}$ , increasing linearly with Gleevec concentration (Figure 3C). The  
183 slope corresponds to the bimolecular rate constant,  $k_2 = (1.1 \pm 0.3) \times 10^6 \text{ M}^{-1}\text{s}^{-1}$ , of Gleevec  
184 binding to Aurora A and the dissociation of Gleevec is determined from the intercept,  $k_{-2} = 31 \pm$   
185  $2 \text{ s}^{-1}$  (Figure 3C). The second, slow phase exhibits an increase in fluorescence intensity (Figure  
186 3A), with the observed rate constant decreasing with Gleevec concentration (Figure 3D). The  
187 decreasing  $k_{obs}$  provides unequivocal evidence of conformational selection, where its rate of  
188 interconversion is slower than the rate of ligand dissociation ( $k_1 + k_{-1} \ll k_{-2}$ ). The values of  $k_1$   
189 and  $k_{-1}$  can be estimated by fitting the data to Equation 1 and are  $0.014 \pm 0.001 \text{ s}^{-1}$  and  $0.011 \pm$   
190  $0.002 \text{ s}^{-1}$ , respectively (Figure 3D). These rate constants represent the conformational change  
191 from DFG-*in* to -*out* and vice versa since Gleevec is a DFG-*out* selective inhibitor due to steric  
192 hindrance (Nagar et al., 2002; Schindler et al., 2000; Seeliger et al., 2007).

193 In order to more rigorously analyze the data and test the model, all time courses of the  
194 fluorescence changes were globally fit using the microscopic rate constants determined above as  
195 starting values (Figure 4) to the model in Figure 3G, where also the resulting microscopic rate  
196 constants are given. The lack of a conformational transition after drug binding (i.e., induced-fit  
197 step) in Aurora A should dramatically decrease drug affinity in comparison to Abl. Indeed, Gleevec  
198 binds to Aurora A with a  $K_D$  of  $24 \pm 7 \text{ }\mu\text{M}$  (Figure 3F) compared to the low nM affinity to Abl  
199 (Agafonov et al., 2014). Two pieces of independent evidence establish that there is indeed no  
200 induced-fit step in Gleevec binding to Aurora A: (i) the calculated  $K_D$  from the kinetic scheme is in  
201 agreement with the macroscopically measured  $K_D$  (*c.f.* Figure 3G and 3F), and (ii) the observed  
202  $k_{off}$  from the dilution experiment (Figure 3E) coincides with the physical dissociation rate (i.e.,  
203 intercept of the binding plot,  $31 \pm 2 \text{ s}^{-1}$ , in Figure 3C). In summary, the lack of an induced-fit step

204 for Gleevec binding to Aurora A is the major reason for Gleevec's weak binding, and not the DFG-  
205 loop conformation.

206

### 207 **Kinetics of Danusertib binding to Aurora A: three-step kinetics with conformational** 208 **selection and an induced-fit step**

209 Next, we wanted to shed light on why Danusertib, unlike Gleevec, binds very tightly to Aurora A.  
210 A high-resolution X-ray structure shows Danusertib bound to Aurora A's active site with its DFG-  
211 loop in the *out* conformation (Figure 5A) (Fancelli et al., 2006), and to rationalize Danusertib's  
212 high affinity we measured the kinetics of Danusertib binding to Aurora A directly by stopped-flow  
213 experiments at 25 °C. An increase in fluorescence intensity was observed at all Danusertib  
214 concentrations and showed double-exponential behavior (Figure 5B). The dependence of the two  
215 observed rates constants on drug concentration is linear for one of them (Figure 5C) and non-  
216 linear for the other with an apparent plateau at approximately  $16 \pm 2 \text{ s}^{-1}$  (Figure 5D). The step with  
217 linear inhibitor concentration dependence corresponds to the second-order binding step, whereas  
218 a non-linear concentration dependency hints at protein conformational transitions. For a  
219 hyperbolic increase of the observed rate with substrate concentrations, one cannot *a priori*  
220 differentiate between a conformational selection and an induced fit mechanism. However,  
221 conformational selection happens before drug binding, and the intrinsic slow DFG-*in* to DFG-*out*  
222 interconversion in Aurora A revealed by Gleevec binding (Figure 3A) must, therefore, be  
223 unaltered. Since the apparent rate of  $16 \pm 2 \text{ s}^{-1}$  (Figure 5D) is two orders of magnitude faster, it  
224 can only reflect an induced-fit step (i.e.,  $k_{obs} = k_3 + k_{-3}$ ).

225 So, what happened to the conformational selection step? We hypothesize that the lack of  
226 this step in our kinetic traces is due to a too small amplitude of this phase, or not observable  
227 because of photobleaching having a bigger effect at the longer measurement times. To lessen  
228 potential photobleaching, we reduced the enzyme concentration and increased the temperature  
229 to 35 °C. Indeed, under these conditions, the slow DFG-*in* to DFG-*out* kinetics were observed as  
230 an increase of fluorescence intensity over time with an observed rate constant of approximately  
231  $0.1 \text{ s}^{-1}$  (Figure 5-figure supplement 1A).

232 While these experiments clearly establish the three-step binding mechanism, it does not  
233 provide accurate rate constants for the conformational selection step and it cannot be observed  
234 at 25 °C where all the other kinetic experiments are performed. To resolve this issue, we repeated  
235 the Aurora A–Gleevec experiment at 25 °C (Figure 5-figure supplement 2A, B) and obtained  
236 reliable rate constants ( $k_1 = 0.09 \pm 0.01 \text{ s}^{-1}$  and  $k_{-1} = 0.06 \pm 0.005 \text{ s}^{-1}$ ) for the conformational  
237 selection step in Aurora A, which will be used as “knowns” in what follows. We hypothesize that

238 the conformational selection step reflects the interconversion between inactive/active  
239 conformations and is correlated with the DFG-*out* and -*in* position (Figure 1). The following  
240 observations support our hypothesis: (i) two crystal structures for the apo-protein show Trp277 in  
241 very different environments (Figure 1E), (ii) Danusertib has been proposed to selectively bind to  
242 the DFG-*out* conformation based on a co-crystal structure (Figure 5A) (Fancelli et al., 2006), and  
243 (iii) the same slow step is observed for binding of both Gleevec and Danusertib.

244 Next, the dissociation kinetics for Danusertib was measured by fluorescence and  
245 appeared to be extremely slow with an observed slow-off rate of  $(3.2 \pm 0.3) \times 10^{-4} \text{ s}^{-1}$  (Figure 5E).  
246 Rationalization of complex binding kinetics cannot be done anymore by visual inspection and  
247 kinetic intuition, which can, in fact, be misleading. In order to elucidate the correct binding  
248 mechanism and obtain accurate kinetic parameters, all kinetic traces were globally fit (Figure 6)  
249 to the three-step binding scheme (Figure 5I). Although global fitting of the binding and dissociation  
250 kinetics in KinTek Explorer delivered a value for  $k_{-2}$ , evaluation of the kinetic scheme with respect  
251 to the time traces exposes that  $k_{-2}$  is not well determined from our experiments. We therefore  
252 designed a double-jump experiment to populate the AurA<sub>out</sub>:D state followed by dissociation to  
253 obtain more accurate information on  $k_{-2}$ . Our stopped-flow machine lacks the capability to  
254 perform double mixing. Therefore, the double-jump experiment was performed using a Creoptix  
255 WAVE instrument. This label-free methodology uses waveguide interferometry to detect refractive  
256 index changes due to alteration in surface mass in a vein similar to Surface Plasmon Resonance  
257 (SPR). It is an orthogonal technique that sidesteps notable issues associated with fluorescence  
258 methods (e.g., photobleaching and inner-filter effects). In short, after immobilizing Aurora A on a  
259 WAVEchip, a high concentration of Danusertib was injected for a short, variable period of time,  
260 and dissociation was triggered by flowing buffer through the microfluidics channel to remove the  
261 drug. The dissociation kinetics fit to a single exponent with a rate constant,  $k_2$ , of  $6.8 \pm 0.4 \text{ s}^{-1}$   
262 (Figure 5F and Figure 5-figure supplement 1B).

263 We want to discuss a few additional kinetic features. First, the observed rate constant  
264 measured in the dilution experiment (Figure 5E,  $k_{-3} = (3.2 \pm 0.3) \times 10^{-4} \text{ s}^{-1}$ ) is slower than  $k_{-3}$   
265 from the global fit ( $k_{-3} = (7.1 \pm 0.5) \times 10^{-4} \text{ s}^{-1}$ ), which might seem counterintuitive. The observed  
266 rate constant was verified by an additional dilution experiment using Creoptix WAVE ( $k_{-3} = (2 \pm$   
267  $0.6) \times 10^{-4} \text{ s}^{-1}$ , Figure 5-figure supplement 1C). The difference in the observed and microscopic  
268 rate constant can, however, be fully reconciled by considering the kinetic partitioning for the  
269 proposed scheme, as shown in Figure 6-figure supplement 1. Second, a powerful and  
270 independent validation of the three-step binding mechanism is obtained by comparing the  
271 measured overall  $K_D$  of Danusertib with the calculated macroscopic  $K_D$  from the microscopic rate



272 constants (Figure 5G, H, I and Figure 5-figure supplement 1D) according to Equation 4, which  
273 indeed delivers values that are within experimental error. In addition, our values for  $k_2$ ,  $k_{-3}$ , and  
274  $K_D$  are in good agreement with those reported in a recent study using SPR (Willemsen-Seegers  
275 et al., 2017).

276 Our results illuminate trivial but profound principles of binding affinity and lifetime of  
277 drug/target complexes: a conformational selection mechanism always weakens the overall  
278 inhibitor affinity, while an induced-fit step tightens the affinity depending on how far-shifted the  
279 equilibrium in the enzyme/drug complex is (Equations 2, 3 and 4). For DFG-*out* binders (e.g.,  
280 Danusertib and Gleevec), the DFG-*in* and -*out* equilibrium weakens the overall affinity 1.6-fold;  
281 however, the conformational change after drug binding results in a four orders of magnitude  
282 tighter binding for Danusertib and is the sole reason for its high affinity to Aurora A compared to  
283 Gleevec. The dissociation constants for the bimolecular binding step  $K_2$  is very similar for both  
284 inhibitors. Finally, the lifetime of Danusertib on the target is very long because of the very slow  
285 conformational dynamics within the Aurora A/Danusertib complex ( $k_{-3} = (7.1 \pm 0.5) \times 10^{-4} \text{ s}^{-1}$ ).

286

### 287 **Kinetics of AT9283 binding to Aurora A – a surprise**

288 We chose AT9283 as a third inhibitor to characterize the binding mechanism because it has been  
289 described as a DFG-*in* binder based on a crystal structure of AT9283 bound to Aurora A (PDB  
290 2W1G, (Howard et al., 2009)). We, therefore, anticipated that in its binding kinetics one can now  
291 detect the DFG-*out* to DFG-*in* switch. Rapid kinetic experiments of binding AT9283 to Aurora A  
292 at 25 °C resulted in biphasic traces and both processes showed an increase in fluorescence over  
293 time (Figure 7A). The  $k_{obs}$  for the faster phase ( $k_2$ ) was linearly dependent on drug concentration  
294 reflecting the binding step (Figure 7B) and  $k_{obs}$  for the slower phase ( $k_3$ ) has a limiting value of  
295  $0.8 \pm 0.2 \text{ s}^{-1}$  and is attributed to an induced-fit step (Figure 7C). For the conformational selection  
296 step (i.e., DFG-*out* to DFG-*in*), a decrease in fluorescence is expected because for the reverse  
297 flip observed in the Gleevec and Danusertib experiments, a fluorescence increase was seen  
298 (Figure 3A and Figure 5-figure supplement 1A). However, we could not find any condition (e.g.,  
299 by varying temperature and ligand concentrations) where such a phase could be observed.

300 Dissociation is characterized by double-exponential kinetics (Figure 7D and Figure 7-  
301 figure supplement 1A). The fast phase (~38% of the total amplitude change) decays with a rate  
302 constant of  $(1.1 \pm 0.02) \times 10^{-2} \text{ s}^{-1}$ , and the slow phase (~62% of the total change in amplitude) has  
303 a rate constant of  $(0.1 \pm 0.01) \times 10^{-2} \text{ s}^{-1}$ . To distinguish between the reverse induced-fit step ( $k_{-3}$ )  
304 and the physical dissociation step ( $k_{-2}$ ), a double-jump experiment was performed that  
305 unambiguously assigned the faster phase to  $k_{-2}$  (Figure 7E and Figure 7-figure supplement 1B).

306 Our attempts to globally fit all kinetic traces assuming binding to only the DFG-*in* state and using  
307 the rate constants for the DFG-loop flip from the Gleevec experiment failed (Figure 8-*figure*  
308 *supplement 1A*). An extended model, where AT9283 can bind to both DFG<sub>in/out</sub> conformations,  
309 followed by a common induced-fit step can also not explain the experimental kinetic traces (Figure  
310 8-*figure supplement 1B*). These failures, together with the lack of a detectable conformational  
311 selection step, led to a new model in which both the DFG-*in* and DFG-*out* states can bind AT9283,  
312 but only AurA<sub>in</sub>:AT can undergo an induced-fit step (Figure 7H). All data can be globally fit to this  
313 model (Figure 8) and the overall  $K_D$  calculated from the corresponding microscopic rate constants  
314 (using Equation 5) is in good agreement with the experimentally measured  $K_D$  (Figure 7F-H).  
315 Finally, the 10-fold difference between the  $k_{-3}$  from the global fit (Figure 7H) and the  
316 experimentally observed slow off-rate can be reconciled by kinetic partitioning as shown in Figure  
317 7-*figure supplement 1A*.

318

### 319 **Crystal structures of AT9283 bound to Aurora A buttress new binding model**

320 In an effort to structurally verify our model we solved a crystal structure of Aurora A with AT9283  
321 bound and indeed observed the DFG-*out* conformation (PDB 6CPG, Figure 9B and Figure 9-  
322 *figure supplement 1*), in contrast to the DFG-*in* conformation as previously reported (Figure 9A)  
323 (Howard et al., 2009). Our structure was obtained by co-crystalizing Aurora A with AT9283 and a  
324 monobody that binds to the same site as the natural allosteric activator TPX2 (Figure 9B). Binding  
325 of this monobody shifts Aurora A into an inactive conformation, with the DFG-loop in the *out*  
326 conformation. This new structure underscores the plasticity of Aurora A kinase and the ability of  
327 AT9283 to bind to a DFG-*out* state, in addition to the previously reported DFG-*in* state.

328 Thus, our structural and kinetic data together support that AT9283 can bind to both DFG-  
329 *in* and DFG-*out* state of Aurora A, and emphasizes the need for caution when interpreting single  
330 X-ray structures.

331

### 332 **Inhibitors take advantage of built-in dynamics for ATP binding**

333 We finally compared the binding kinetics of the ATP-competitive inhibitors described above with  
334 the natural kinase substrate, ATP (Figure 10). In order to measure stopped-flow kinetics for ATP  
335 binding, FRET was measured by exciting Trp residues in Aurora A and detecting fluorescence  
336 transfer to the ATP-analogue mant-ATP (Lemaire, Tessmer, Craig, Erie, & Cole, 2006; Ni,  
337 Shaffer, & Adams, 2000). The binding of mant-ATP to Aurora A showed biphasic kinetic traces  
338 (Figure 10A) that describe the physical binding step (i.e., linear dependence on mant-ATP  
339 concentration; Figure 10B) and the induced-fit step (Figure 10C). The observed rate constant



340 approaches a maximum value defined by the sum of  $k_3 + k_{-3}$  (Figure 10C) and the intercept can  
341 be estimated to be  $k_{-3}$  and is consistent with the value obtained from the  $k_{off}$  experiment (Figure  
342 10D). We find that mant-ATP can bind to both the DFG-*in* or -*out* conformations, consistent with  
343 our nucleotide-bound crystal structures (Figure 1A-D) and recent single-molecule fluorescence  
344 spectroscopy data that indicates that nucleotide binding does not significantly affects this  
345 equilibrium (Gilbert et al., 2017). To confirm the model, the kinetic data were globally fit to a two-  
346 step binding mechanism (Figure 10H, G). The calculated  $K_D$  from the corresponding microscopic  
347 rate constants (Figure 10H) is comparable with experimental macroscopic  $K_D$  obtained from a  
348 titration experiment (Figure 10E, F).

349 The presence of an induced-fit step for the natural substrate ATP suggests that such  
350 conformational change after ligand binding is a built-in property of the enzyme. In other words,  
351 inhibitors take advantage of the inherent plasticity of the enzyme that is required for its activity  
352 and regulation. The main difference between ATP and inhibitor binding is the rate constant for the  
353 reverse induced-fit step ( $k_{-3}$ ). In the case of ATP, this rate is much faster and, therefore, does  
354 not significantly increase the overall affinity. Faster conformational changes and weaker binding  
355 are of course prerequisites for efficient turnover; whereas slow conformational changes,  
356 particularly the reverse induced-fit step, are at the heart of action for an efficient drug, because it  
357 results in tight binding and a long lifetime on the target. In summary, binding of different ligands  
358 to the ATP-binding site, such as nucleotides or ATP-competitive inhibitors, is comprised of the  
359 physical binding step followed by an induced-fit step. By definition, it is the nature of the induced-  
360 fit step that varies for the different ligands since it happens as a result of ligand binding.

361

## 362 Discussion

363 Characterizing the detailed kinetic mechanisms of drug binding is not just an academic exercise  
364 but delivers fundamental knowledge for developing selective inhibitors with high affinity. An  
365 induced-fit step turns out to be key for all tight-binding inhibitors studied. From our results on  
366 Aurora A kinase presented here and earlier data on Tyrosine-kinases (Agafonov et al., 2014;  
367 Wilson et al., 2015), we propose that this is a general mechanism for different kinases and multiple  
368 inhibitors, thereby providing a platform for future computational and experimental efforts in rational  
369 drug design.

370 The “use” of a far-shifted induced-fit step for a promising drug is logical for the following  
371 reasons: (i) it increases the affinity for the drug by this coupled equilibrium, (ii) it prolongs the  
372 residence time of the drug on the target due to the often slow reverse rate, (iii) it is specific for  
373 each drug as it happens after the drug binding, and (iv) it can add selectivity for the targets

374 because it likely involves residues more remote from the active site. An increased drug residence  
375 time has significant pharmacological advantages as it can lead to a prolonged biological effect, a  
376 decrease of side effects, and a lower risk of metabolic drug modification. Such inhibitors have  
377 long been described as slow tight-binding inhibitors (Copeland, 2016; Copeland, Pompliano, &  
378 Meek, 2006). The concept of the advantageous roles of induced-fit steps is based on simple  
379 thermodynamics and protein flexibility, and is, therefore, likely of relevance for drug design to  
380 other targets outside of the kinome.

381         Additionally, our data provides unique insight into the extensively discussed DFG flip.  
382 Combining x-ray crystallography, NMR spectroscopy and stopped-flow kinetics of drug binding  
383 establish the nature of this DFG flip both structurally, thermodynamically and kinetically, and  
384 resolves the longstanding question of its role for drug affinity and selectivity. Selective binding of  
385 a specific DFG-state by Gleevec has been first proposed as the reason for selectivity towards Abl.  
386 This conformational selection principle has ever since been at the center of drug discovery for  
387 many kinases, including Aurora A (Badrinarayan & Sastry, 2014; Liu & Gray, 2006). Based on our  
388 results, we argue that conformational selection of the DFG-state by ATP-competitive inhibitors is  
389 a mistakenly pursued concept in drug design for the following reasons: (i) conformational selection  
390 by definition weakens the overall ligand affinity, (ii) active site binders are automatically inhibitors,  
391 therefore selective binding to a specific DFG-state has no advantage (Badrinarayan & Sastry,  
392 2014; Liu & Gray, 2006), (iii) kinases interconvert between both states. High selectivity gained by  
393 DFG-state selective binding could only be achieved in the scenario of a highly skewed population  
394 towards the binding-competent state for one kinase relative to all others, which is unfounded.

395         Our results exemplify why rational drug design is so challenging. The characterization of  
396 the complete free-energy landscape of drug binding is needed, which will require more  
397 sophisticated computational approaches guided by experimental data such as provided in our  
398 study. A good illustration of this point are the computational reports that focused on the DFG flip  
399 as a key determinant drug selectivity (Badrinarayan & Sastry, 2014) that now have been ruled out  
400 by our kinetic measurements. Our data suggest that future design efforts should be focusing on  
401 understanding and exploiting induced-fit steps. The findings presented here are encouraging for  
402 developing selective inhibitors even for kinases with very similar folds and drug binding pockets  
403 since the action does not happen on a single structural element of the protein but, on a complex  
404 energy landscape that is unique to each kinase.

405

406

407

## 408 **Materials and Methods**

409

### 410 **Cloning, expression and purification of dephosphorylated Aurora A (122-403) and** 411 **inhibiting monobody.**

412 Dephosphorylated Aurora A proteins were expressed and purified as described before (Zorba et  
413 al., 2014) and analyzed by mass spectrometry to confirm their phosphorylation state. The W227L  
414 mutant was generated using the QuickChange Lightning site-directed mutagenesis kit (Agilent).

415 U-[<sup>15</sup>N] Aurora A was obtained by growing *E. coli* in M9 minimal medium containing 1 g/L  
416 <sup>15</sup>NH<sub>4</sub>Cl (Cambridge Isotope Laboratories, Tewksbury, MA, USA) and 5 g/L D-glucose as the sole  
417 nitrogen and carbon source, respectively. [<sup>15</sup>N]-Trp labeled wild-type Aurora A was obtained using  
418 the standard M9 minimal medium, complemented with all amino acids (0.5 g/L) with the exception  
419 of tryptophan. One hour prior to induction, 30 mg/L of <sup>15</sup>N<sub>2</sub>-L-Trp (NLM-800; Cambridge Isotope  
420 Laboratories, Tewksbury, MA, USA) was added to the medium. Similarly, to obtain samples of  
421 wild-type and W277L Aurora A containing 5-fluoro-tryptophan, bacterial growth was performed in  
422 unlabeled M9 medium containing all amino acids (0.5 g/L) except for tryptophan. One hour before  
423 protein induction, the media was supplemented with 30 mg/L of 5-fluoro-DL-tryptophan (Sigma-  
424 Aldrich) (Crowley, Kyne, & Monteith, 2012). NMR samples contained 200-300 μM Aurora A in 50  
425 mM HEPES, pH 7.3, 50 mM NaCl, 20 mM MgCl<sub>2</sub>, 5 mM TCEP, 2 M TMAO and 10%(v/v) D<sub>2</sub>O.

426 Inhibiting monobody used for co-crystallization with Aurora A and AT9283 was expressed  
427 in *E. coli* BL21(DE3) cells harboring the plasmid pHBT containing His<sub>6</sub>-tagged-Mb. A culture of  
428 TB media containing 50 μg/mL kanamycin that was grown overnight at 37 °C was added to 1L of  
429 TB media with 50 μg/mL kanamycin to get a starting OD<sub>600</sub> of ~0.2. This culture was grown at 37  
430 °C until the OD<sub>600</sub> reached ~0.8. Protein expression was induced by 0.6 mM IPTG at 18 °C for  
431 13-15 h and cells were harvested by centrifugation. The cell pellet was resuspended in binding  
432 buffer (50 mM Tris-HCl, pH 8.0, 300 mM NaCl, 20 mM imidazole, 20 mM MgCl<sub>2</sub>, 10% glycerol)  
433 containing 0.5 mg/mL lysozyme, 5 μg/mL DNase, and 1x EDTA-free protease inhibitor cocktail.  
434 Cells were ruptured by sonication on ice then centrifuged at 18,000 rpm at 4 °C for 1 h. The  
435 supernatant was loaded onto HisTrap<sup>TM</sup> HP (GE Healthcare) after filtration using 0.22 μm filtering  
436 unit. The pellet was resuspended with GuHCl buffer (20 mM Tris-HCl, pH 8.0, 6 M GuHCl) and  
437 allowed to rotate on wheel for 10 min at 4 °C and spun down again. The supernatant was passed  
438 through 0.2 μm filtering unit and loaded onto HisTrap<sup>TM</sup> HP column previously loaded with soluble  
439 fraction and pre-equilibrated with GuHCl buffer. Refolding monobody on-column was achieved by  
440 washing the HisTrap<sup>TM</sup> HP column with 5 column volumes (CV) of GuHCl buffer, followed by 5

441 CV of Triton-X buffer (binding buffer + 0.1% Triton X-100), then 5 CV of  $\beta$ -cyclodextrin buffer  
442 (binding buffer + 5 mM  $\beta$ -cyclodextrin), and finally 5 CV of binding buffer. Monobody was eluted  
443 with 100% of elution buffer (binding buffer + 500 mM imidazole). The protein was dialyzed  
444 overnight in gel-filtration buffer (20 mM Tris-HCl, pH 7.5, 200 mM NaCl, 20 mM MgCl<sub>2</sub>, 5 mM  
445 TCEP, 10% glycerol) in the presence of TEV protease (1:40 TEVP:Mb molar ratio). After dialysis,  
446 the TEV-cleaved monobody was passed through HisTrap™ HP column again. The flow-through  
447 containing TEV-cleaved monobody was collected and concentrated before loading onto Superdex  
448 200 26/60 gel-filtration column pre-equilibrated with the gel-filtration buffer. The monobody was  
449 flash-frozen and stored in -80 °C until use.

450

### 451 **X-ray crystallography**

452 Crystals of dephosphorylated (deP) Aurora A<sup>122-403</sup> + AMPPCP were obtained by mixing 570  $\mu$ M  
453 (18 mg/mL) deP Aurora A<sup>122-403</sup> and 1 mM AMPPCP in a 2:1 ratio with mother liquor (0.2 M  
454 ammonium sulfate, 0.2 M Tris-HCl, pH 7.50, 30% (w/v) PEG-3350). The crystals were grown at  
455 18 °C by vapor diffusion using the hanging-drop method. The protein used for the crystallization  
456 was in storage buffer (20 mM Tris-HCl, pH 7.5, 200 mM NaCl, 10% (v/v) glycerol, 20 mM MgCl<sub>2</sub>,  
457 1 mM TCEP); AMPPCP was freshly prepared before use in the same buffer. Crystals were flash-  
458 frozen in liquid nitrogen prior to shipping. Crystals of apo, deP Aurora A<sup>122-403</sup> were grown at 18  
459 °C by vapor diffusion using the sitting-drop method (96-well plate). A 1:1 ratio of protein to mother  
460 liquor was obtained by combining 0.5  $\mu$ L of 300  $\mu$ M (10 mg/mL) deP Aurora A<sup>122-403</sup> in 50 mM  
461 HEPES, pH 7.3, 500 mM ammonium acetate, 1 mM MgCl<sub>2</sub>, 5 mM TCEP) with 0.5  $\mu$ L of 0.15 M  
462 Tris-HCl, pH 7.5, 0.15 M ammonium sulfate, 35% (w/v) PEG-3350. Crystals were soaked for 10-  
463 20 s in cryo buffer (20% (w/v) PEG-400, 20% ethylene glycol, 10% water and 50% mother liquor)  
464 before flash-freezing in liquid nitrogen. The complex between Aurora A<sup>122-403</sup>, inhibiting monobody  
465 (Mb) and AT9283 was crystallized at 18 °C by vapor diffusion using the sitting-drop method. In  
466 short, a 1:1 ratio of protein mixture to mother liquor was obtained by combining 0.5  $\mu$ L of sample  
467 [240  $\mu$ M deP Aurora A<sup>122-403</sup> + 1.0 mM AT9283 + 250  $\mu$ M Mb] with 0.5  $\mu$ L of mother liquor [0.1 M  
468 Bis-Tris, pH 5.5, 0.2 M magnesium chloride, 19% (w/v) PEG-3350]. Crystals were soaked for 10-  
469 20 s in cryo buffer (17.5% (w/v) PEG-400, 17.5% ethylene glycol, 45% water and 20% mother  
470 liquor) before flash-freezing in liquid nitrogen.

471 Diffraction data were collected at 100 K at the Advanced Light Source (Lawrence Berkeley  
472 National Laboratory) beamlines ALS 8.2.1 (apo-AurA and AurA+Mb+AT9283) and 8.2.2  
473 (AurA+AMPPCP) with a collection wavelength of 1.00 Å.

474 Data were indexed and integrated using iMOSFLM (Battye, Kontogiannis, Johnson,

475 Powell, & Leslie, 2011) for apo/AMPPCP-bound Aurora A and Xia2 (Winter, 2010) using XDS  
476 (Kabsch, 2010) for the Aurora A/Mb/AT9283 complex, respectively. Data were scaled and merged  
477 with AIMLESS (Evans & Murshudov, 2013), in the case of Aurora A/Mb/AT9283 two data separate  
478 data sets were merged. All software was used within the CCP4 software suite (Winn et al., 2011).

479 As initial search models 1MQ4 (Nowakowski et al., 2002) and 3K2M (Wojcik et al., 2010)  
480 were used for Aurora A and monobody, respectively, and molecular replacement was performed  
481 using Phaser (McCoy et al., 2007). The molecules were placed in the unit cell using the  
482 ACHESYM webserver (Kowiel, Jaskolski, & Dauter, 2014). Iterative refinements were carried out  
483 with PHENIX (Adams et al., 2010), using rosetta.refine (DiMaio et al., 2013) and phenix.refine  
484 (Afonine et al., 2012), and manual rebuilding was performed in Coot (Emsley & Cowtan, 2004;  
485 Emsley, Lohkamp, Scott, & Cowtan, 2010).

486 Structure validation was performed using MolProbity (V. B. Chen et al., 2010) and yielded  
487 the statistics given below. The Ramachandran statistics for dephosphorylated apo (AMPPCP-  
488 bound) Aurora A are: favored: 93.65 (94.90)%, allowed 5.95 (4.71)%, outliers: 0.4 (0.39)%; 0.48  
489 (0.0)% rotamer outliers and an all-atom clashscore of 4.45 (2.44). For the Aurora A/Mb/AT9283  
490 complex, the Ramachandran statistics are: favored: 92.64%, allowed 7.06%, outliers: 0.3%); 0.0  
491 % rotamer outliers and an all-atom clashscore of 2.81. We note that the B-factors for the  
492 monobodies in the complex of Aurora A/Mb/AT9283 are rather high, indicating significantly  
493 flexibility in the parts that are not part of the binding interface with Aurora A.

494 The data collection and refinement statistics are given in Figure 1-*figure supplement 1* and  
495 Figure 9-*figure supplement 1*. Structure factors and refined models have been deposited in the  
496 PDB under accession codes: 6CPE (apo Aurora A), 6CPF (Aurora A + AMPPCP) and 6CPG  
497 (Aurora A/Mb/AT9283).

498

499 All figures were generated using Chimera (Pettersen et al., 2004).

500

## 501 **NMR spectroscopy**

502 All  $^{19}\text{F}$  NMR experiments were performed at 35 °C on a Varian Unity Inova 500 MHz spectrometer,  
503 equipped with a  $^1\text{H}/^{19}\text{F}$  switchable probe tuned to fluorine (90° pulse width of 12  $\mu\text{s}$ ). All 1D  $^{19}\text{F}$   
504 spectra were recorded with a spectral width of ~60 ppm and a maximum evolution time of 0.25 s.  
505 An interscan delay of 1.5 s was used with 5,000 scans per transients, giving rise to a total  
506 acquisition time of 2.5 h per spectrum. To remove background signal from the probe and avoid  
507 baseline distortions, data acquisition was started after a ~100  $\mu\text{s}$  delay (using the "delacq" macro)  
508 and appropriate shifting of the data followed by backward linear prediction was performed. The

509 data were apodized with an exponential filter (2.5 Hz line broadening) and zero-filled before  
510 Fourier transform. To improve the signal-to-noise ratio several data sets were recorded  
511 consecutively and, provided that the sample remained stable, added together after processing  
512 (two for apo Aurora A, four for Aurora A + AMPPCP, and five for W277L + AMPPCP, respectively).  
513  $^{19}\text{F}$  chemical shifts were referenced externally to trifluoroacetic acid (TFA) at -76.55 ppm.

514  $[^1\text{H}-^{15}\text{N}]$ -TROSY-HSQC experiments were recorded at 25 °C on an Agilent DD2 600 MHz  
515 four-channel spectrometer equipped with a triple-resonance cryogenically cooled probe-head.  
516 Typically, 115–128 ( $^{15}\text{N}$ )  $\times$  512 ( $^1\text{H}$ ) complex points, with maximum evolution times equal to 48.5–  
517 64 ( $^{15}\text{N}$ )  $\times$  64 ( $^1\text{H}$ ) ms. An interscan delay of 1.0 s was used along with 32 or 56 scans per transient,  
518 giving rise to a net acquisition time 1.5-2.5 h for each experiment. To improve the signal-to-noise  
519 ratio several data sets were recorded consecutively and, provided that the sample remained  
520 stable, added together after processing (typically three data sets per sample).

521 All data sets were processed with the NMRPipe/NMRDraw software package (Delaglio et  
522 al., 1995) and 2D spectra were visualized using Sparky (Goddard, 2008). Deconvolution of the  
523  $^{19}\text{F}$  spectra and line shape fitting was performed using the Python package nmrglue (Helmus &  
524 Jaroniec, 2013).

525

### 526 **Kinetics experiments of Aurora A with Gleevec, Danusertib, and AT9283**

527 **Stopped-flow experiment.** Intrinsic tryptophan fluorescence spectroscopy was used to monitor  
528 drug binding kinetics to Aurora A. All experiments were performed at 25 °C, except for the Gleevec  
529 kinetics that were measured at 10 °C (unless otherwise stated) because the binding of Gleevec  
530 to Aurora A is too fast  $k_{\text{obs, Binding}}$ . Stock solutions of 200 mM Danusertib, 200 mM AT9283 and  
531 50 mM Gleevec (all purchased from Selleck Chemicals) were prepared in 100% DMSO and  
532 stored at -80 °C until used. Aurora A used in the kinetic experiments was dephosphorylated  
533 Aurora A as determined by mass spectrometry, Western blot and activity experiments (data not  
534 shown). The rapid kinetics were studied using a stopped-flow spectrophotometer (SX20 series  
535 from Applied Photophysics Ltd). The flow system was made anaerobic by rinsing with degassed  
536 buffer comprised of 50 mM HEPES, 50 mM NaCl, 20 mM  $\text{MgCl}_2$ , 5 mM TCEP, 5% DMSO, pH  
537 7.30 to minimize photobleaching. The stock solutions of Aurora A and all drugs were made  
538 anaerobic by degassing with ThermoVac (MicroCal) at the desired temperature. In general, a  
539 solution of 5  $\mu\text{M}$  Aurora A was loaded in one syringe and quickly mixed with drug, prepared in the  
540 same buffer, in the other syringe (mixing ratio 1:10). A significant increase or decrease in the  
541 fluorescence intensity of Aurora A (excitation at 295 nm, emission cut-off at 320 nm) can be  
542 observed due to the drug binding. For each drug concentration, at least five replicate



543 measurements were made and these transients were averaged. Analysis was performed by fitting  
544 the individual trace to exponential equations using Pro-Data Viewer (Applied Photophysics Ltd)  
545 or with Kinesyst 3 software (TgK Scientific) and error bars denote the standard errors as obtained  
546 from the fit. KaleidaGraph version 4.5.3 (Synergy) was used for data analysis and plotting. All  
547 kinetic data were globally fitted in KinTek Explorer software (Johnson, 2009; Johnson, Simpson,  
548 & Blom, 2009).

549 Under the rapid equilibrium approximation, the binding and dissociation steps of Gleevec  
550 to Aurora A are fast compared to conformational selection, therefore the value of  $k_1$  and  $k_{-1}$  can  
551 be estimated according to Equation 1:

552

$$k_{obs} = \frac{k_{-1}}{1 + \left( \frac{[Gleevec]}{[Aurora A] + \left( \frac{k_{-2}}{k_2} \right)} \right)} + k_1 \quad \text{Equation 1}$$

553

554

555 where  $k_1$  and  $k_{-1}$  represent the conformational change from DFG-*in* to -*out* and vice versa,  
556 respectively. The approximate values of  $k_1$  and  $k_{-1}$  obtained from fitting to this equation are used  
557 as starting values for the global fit.

558 For the 5  $\mu$ M Aurora A/Gleevec complex, the release of the drug was recorded after a 11-  
559 fold dilution of the complex using the stopped-flow instrument for 0.25 s (excitation at 295 nm,  
560 emission cut-off at 320 nm) at 10 °C.

561

562 **Creoptix WAVE experiments.** Double jump, slow-off, and macroscopic  $K_D$  experiments of  
563 Aurora A with drugs were studied using a Creoptix WAVE instrument (Creoptix AG, Wädenswil,  
564 Switzerland) at 25 °C. All chemicals were purchased from GE Healthcare, unless otherwise  
565 stated. The protocols in the WAVEcontrol software for conditioning of the chip, immobilization of  
566 proteins and performing kinetics experiments were followed. In short, the polycarboxylate chip  
567 (PCH) was activated by injection of a 1:1 mixture with final concentrations of 200 mM N-ethyl-N'-  
568 (3-dimethylaminopropyl)carbodiimide (EDC) and 50 mM N-hydroxysuccinimide (NHS), followed  
569 by streptavidin immobilization (50  $\mu$ g/mL in 10 mM sodium acetate pH 5.0). Unreacted sites on  
570 the chip were blocked with 1 M ethanolamine pH 8.0. For all activation, immobilization and  
571 passivation steps 0.2x HBS-EP was used as running buffer with a flowrate of 10  $\mu$ L/min and an  
572 injection duration of 420 s on both channels 1 and 2.

573 Biotinylated T288V variant that mimics dephosphorylated Aurora A was used for  
574 experiments performed on the Creoptix WAVE instrument. The activity of T288V with substrate

575 Lats2, the macroscopic  $K_D$  and slow-off rate of Danusertib were the same as wild-type (data not  
576 shown). Biotinylated T288V Aurora A (70  $\mu\text{g/mL}$ ) was immobilized on the PCH-streptavidin chip  
577 with 10  $\mu\text{L/min}$  injection and 15 s injection duration over channel 1 only (channel 2 was used as  
578 reference channel). All experiments were run in 50 mM HEPES, 50 mM NaCl, 20 mM  $\text{MgCl}_2$ , 5  
579 mM TCEP, 0.03 mg/mL BSA, 0.005% Tween-20, pH 7.30 as running buffer. Binding experiments  
580 were evaluated over a range of Danusertib (0.13 – 66.67 nM), AT9283 (0.03 – 64.8 nM), and  
581 Gleevec (0.37 – 40  $\mu\text{M}$ ) concentrations. Gleevec binding experiments contained 5% DMSO in the  
582 running buffer (see above) to enhance Gleevec's solubility. Double-jump experiments of Aurora  
583 A/drugs were performed by injecting 1  $\mu\text{M}$  Danusertib or AT9283 with 0.2, 0.4, 0.8, and 2 s  
584 injection duration for Danusertib and 1 and 3 s injection duration for AT9283 followed by a 60 s  
585 dissociation duration per injection. The slow-off experiments were performed by injecting 5  $\mu\text{M}$   
586 Danusertib or AT9283 with 5-10 s injection duration (to fully saturate Aurora A) followed by a 180  
587 s injection of buffer to remove the excess drug and the dissociation was measured for a duration  
588 of 10800 s.

589  
590 **Spectrofluorometer experiments.** The spectrofluorometer FluoroMax-4 (Horiba Scientific) with  
591 temperature controller was used to study the slow-off rate of Aurora A with Danusertib at 25  $^\circ\text{C}$ .  
592 For this experiment, a solution containing 30 nM Aurora A and 30 nM Danusertib was pre-  
593 incubated for an hour, before diluting 30-fold into degassed buffer (ratio 1:30). A significant  
594 decrease in the fluorescence intensity of Aurora A (excitation at 295 nm, emission at 340 nm) can  
595 be seen due to the Danusertib release. The fluorescence signal was recorded every 160 s for a  
596 duration of six hours using the photobleaching minimization option that will close the shutter after  
597 each acquisition. A control experiment was performed, using the same experimental conditions,  
598 but without drug in order to account for photobleaching.

599  
600 **Overall dissociation constant calculated from intrinsic rate constants.** In the following  
601 equations,  $K_1$ ,  $K_2$ ,  $K_3$  and  $K_4$  equal to:

602 
$$K_1 = \frac{k_{-1}}{k_1}$$

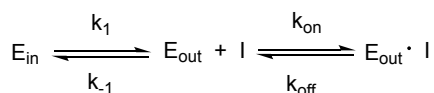
603 
$$K_2 = \frac{k_{-2}}{k_2} = \frac{k_{off}}{k_{on}}$$

604 
$$K_3 = \frac{k_{-3}}{k_3}$$

605 
$$K_4 = \frac{k_{-4}}{k_4}$$



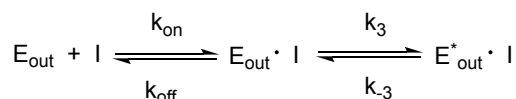
606 Conformational selection followed by inhibitor binding:



607  $K_1$   $K_2$   $K_D = (K_1 + 1) \cdot K_2$  Equation 2

608

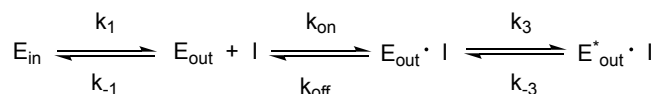
609 Inhibitor binding followed by an induced-fit step:



610  $K_2$   $K_3$   $K_D = \frac{K_2 \cdot K_3}{(K_3 + 1)}$  Equation 3

611

612 Conformational selection followed by inhibitor binding and an induced-fit step:



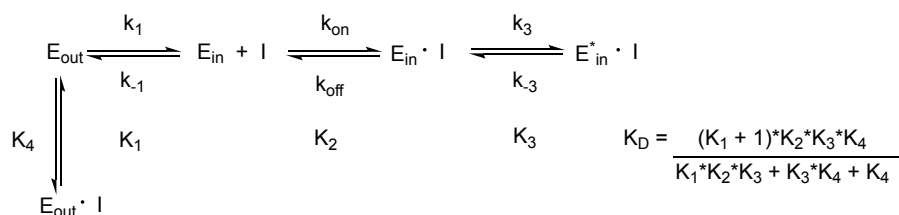
613  $K_1$   $K_2$   $K_3$   $K_D = \frac{(K_1 + 1) \cdot K_2 \cdot K_3}{(K_3 + 1)}$  Equation 4

614

615 Conformational selection mechanism, followed by inhibitor binding to both DFG-*in* and -*out* state,

616 but an induced-fit step only occurs in the DFG-*in* state:

617



618  $K_1$   $K_2$   $K_3$   $K_D = \frac{(K_1 + 1) \cdot K_2 \cdot K_3 \cdot K_4}{K_1 \cdot K_2 \cdot K_3 + K_3 \cdot K_4 + K_4}$  Equation 5

619

620 The uncertainties in the calculated dissociation constant parameter using the equations above

621 are obtained using standard error propagation.

622

623 **Aurora A binding to mant-ATP.** FRET using intrinsic tryptophan fluorescence is used to monitor

624 mant-ATP binding kinetics to Aurora A at 10 °C. In the binding experiment or  $k_{on}$ , increasing

625 concentration of mant-ATP were quickly mixed to 0.5 μM Aurora A (ratio 1:10, excitation at 295

626 nm, emission cut-off at 395 nm). In the experiment to measure the release of mant-ATP or  $k_{off}$ ,

627 10  $\mu\text{M}$ /10  $\mu\text{M}$  Aurora A/mant-ATP complex was diluted with buffer (ratio 1:10). A significant  
628 decrease in the fluorescence intensity of Aurora A (excitation at 295 nm, emission cut-off at 395  
629 nm) can be seen due to the mant-ATP release.

630

### 631 **Macroscopic dissociation constant experiments**

632 Fluorescence titration experiments were measured using FluoroMax-4 spectrofluorometer  
633 (Horiba Scientific). Increasing amounts of Aurora A/Danusertib complex (4 nM Aurora A and 150  
634 nM Danusertib) or Aurora A/mant-ATP (1  $\mu\text{M}$  Aurora A and 2 mM mant-ATP) were titrated into an  
635 Aurora A solution (4 nM and 1  $\mu\text{M}$  Aurora A for experiments with Danusertib and mant-ATP,  
636 respectively). To measure Danusertib affinity, the excitation wavelength was 295 nm (5 nm  
637 bandwidth) and emission spectra were recorded from 310–450 nm (20 nm bandwidth) in  
638 increments of 2 nm and the temperature was maintained at 25 °C. For the mant-ATP experiment,  
639 the dissociation constant was measured at 10 °C using fluorescence energy transfer from  
640 tryptophan residues in Aurora A to mant-ATP by setting the excitation wavelength to 290 nm (5  
641 nm bandwidth) and collecting the emission intensity from 310–550 nm (5 nm bandwidth) in  
642 increments of 2 nm. A control experiment in the absence of Aurora A was performed using the  
643 same experimental settings and used to correct for the mant-ATP interference. In all experiments,  
644 a 5 minutes equilibration time was used after each addition of Aurora A/Danusertib complex or  
645 Aurora A/mant-ATP complex.

646 The fluorescence intensity at 368 nm versus Danusertib concentration or the change in  
647 fluorescence at 450 nm ( $\Delta F^{450}$ ) versus mant-ATP concentration was fitted to Equation 6 using  
648 Marquardt-Levenberg nonlinear fitting algorithm included in KaleidaGraph to obtain the  $K_D$ .

649

$$650 \quad F = F_0 + A \cdot \frac{[I] + [E_t] + K_D - \sqrt{([I] + [E_t] + K_D)^2 - 4 \cdot [E_t] \cdot [I]}}{2 \cdot [E_t]} \quad \text{Equation 6}$$

651

652 F and  $F_0$  are the fluorescence and initial fluorescence intensities, respectively. [I] and  $[E_t]$  are the  
653 total concentration of the drug or mant-ATP and the Aurora A, respectively.

654

### 655 **Acknowledgments**

656 We thank C. Sasseti (University of Massachusetts Medical School, Worcester) for the use of the  
657 ESI-Q-TOF instrument, and the Advanced Light Source (ALS), Berkeley, CA, USA, for access to  
658 beamlines BL8.2.1. and BL8.2.2. The Berkeley Center for Structural Biology is supported in part  
659 by the National Institutes of Health, National Institute of General Medical Sciences, and the HHMI.

660 The ALS is supported by the Director, Office of Science, Office of Basic Energy Sciences, of the  
661 U.S. Department of Energy under contract DE-AC02-05CH11231. We thank Shohei and Akiko  
662 Koide (New York University) for the plasmid of the monody used here. This work was supported  
663 by the Howard Hughes Medical Institute (HHMI); the Office of Basic Energy Sciences, Catalysis  
664 Science Program, U.S. Dept. of Energy (award DE-FG02-05ER15699); and the NIH (grant  
665 GM100966-01). R.O. was a HHMI Fellow of the Damon Runyon Cancer Research Foundation  
666 (DRG-2114-12).

667

### 668 **Competing interests**

669 All authors declare no competing financial or other interests.

670

671

672

673

### References

674

675 Adams, P. D., Afonine, P. V., Bunkoczi, G., Chen, V. B., Davis, I. W., Echols, N., . . . Zwart, P. H.  
676 (2010). PHENIX: a comprehensive Python-based system for macromolecular  
677 structure solution. *Acta Crystallogr D Biol Crystallogr*, 66(Pt 2), 213-221.  
678 doi:10.1107/S0907444909052925

679 Afonine, P. V., Grosse-Kunstleve, R. W., Echols, N., Headd, J. J., Moriarty, N. W., Mustyakimov,  
680 M., . . . Adams, P. D. (2012). Towards automated crystallographic structure refinement  
681 with phenix.refine. *Acta Crystallogr D Biol Crystallogr*, 68(Pt 4), 352-367.  
682 doi:10.1107/S0907444912001308

683 Agafonov, R. V., Wilson, C., Otten, R., Buosi, V., & Kern, D. (2014). Energetic dissection of  
684 Gleevec's selectivity toward human tyrosine kinases. *Nat Struct Mol Biol*, 21(10), 848-  
685 853. doi:10.1038/nsmb.2891

686 Asteriti, I. A., Daidone, F., Colotti, G., Rinaldo, S., Lavia, P., Guarguaglini, G., & Paiardini, A.  
687 (2017). Identification of small molecule inhibitors of the Aurora-A/TPX2 complex.  
688 *Oncotarget*, 8(19), 32117-32133. doi:10.18632/oncotarget.16738

689 Badrinarayan, P., & Sastry, G. N. (2014). Specificity rendering 'hot-spots' for aurora kinase  
690 inhibitor design: the role of non-covalent interactions and conformational transitions.  
691 *PLoS One*, 9(12), e113773. doi:10.1371/journal.pone.0113773

692 Barakat, K. H., Huzil, J. T., Jordan, K. E., Evangelinos, C., Houghton, M., & Tuszynski, J. (2013).  
693 A computational model for overcoming drug resistance using selective dual-  
694 inhibitors for aurora kinase A and its T217D variant. *Mol Pharm*, 10(12), 4572-4589.  
695 doi:10.1021/mp4003893

696 Battye, T. G., Kontogiannis, L., Johnson, O., Powell, H. R., & Leslie, A. G. (2011). iMOSFLM: a  
697 new graphical interface for diffraction-image processing with MOSFLM. *Acta*  
698 *Crystallogr D Biol Crystallogr*, 67(Pt 4), 271-281. doi:10.1107/S0907444910048675

699 Bavetsias, V., & Linardopoulos, S. (2015). Aurora Kinase Inhibitors: Current Status and  
700 Outlook. *Front Oncol*, 5, 278. doi:10.3389/fonc.2015.00278

- 701 Bavetsias, V., Perez-Fuertes, Y., McIntyre, P. J., Atrash, B., Kosmopoulou, M., O'Fee, L., . . . Blagg,  
702 J. (2015). 7-(Pyrazol-4-yl)-3H-imidazo[4,5-b]pyridine-based derivatives for kinase  
703 inhibition: Co-crystallisation studies with Aurora-A reveal distinct differences in the  
704 orientation of the pyrazole N1-substituent. *Bioorg Med Chem Lett*, 25(19), 4203-4209.  
705 doi:10.1016/j.bmcl.2015.08.003
- 706 Bayliss, R., Burgess, S. G., & McIntyre, P. J. (2017). Switching Aurora-A kinase on and off at an  
707 allosteric site. *FEBS J*, 284(18), 2947-2954. doi:10.1111/febs.14069
- 708 Bayliss, R., Sardon, T., Vernos, I., & Conti, E. (2003). Structural basis of Aurora-A activation  
709 by TPX2 at the mitotic spindle. *Molecular Cell*, 12(4), 851-862. doi:10.1016/S1097-2765(03)00392-7  
710
- 711 Borisa, A. C., & Bhatt, H. G. (2017). A comprehensive review on Aurora kinase: Small molecule  
712 inhibitors and clinical trial studies. *Eur J Med Chem*, 140, 1-19.  
713 doi:10.1016/j.ejmech.2017.08.045
- 714 Burgess, S. G., Oleksy, A., Cavazza, T., Richards, M. W., Vernos, I., Matthews, D., & Bayliss, R.  
715 (2016). Allosteric inhibition of Aurora-A kinase by a synthetic vNAR domain. *Open  
716 Biol*, 6(7). doi:10.1098/rsob.160089
- 717 Campos-Olivas, R., Marenchino, M., Scapozza, L., & Gervasio, F. L. (2011). Backbone  
718 assignment of the tyrosine kinase Src catalytic domain in complex with imatinib.  
719 *Biomol NMR Assign*, 5(2), 221-224. doi:10.1007/s12104-011-9304-7
- 720 Carpinelli, P., Ceruti, R., Giorgini, M. L., Cappella, P., Gianellini, L., Croci, V., . . . Moll, J. (2007).  
721 PHA-739358, a potent inhibitor of Aurora kinases with a selective target inhibition  
722 profile relevant to cancer. *Mol Cancer Ther*, 6(12 Pt 1), 3158-3168. doi:10.1158/1535-  
723 7163.MCT-07-0444
- 724 Carvajal, R. D., Tse, A., & Schwartz, G. K. (2006). Aurora kinases: new targets for cancer  
725 therapy. *Clin Cancer Res*, 12(23), 6869-6875. doi:10.1158/1078-0432.CCR-06-1405
- 726 Cheetham, G. M., Knechtel, R. M., Coll, J. T., Renwick, S. B., Swenson, L., Weber, P., . . . Austen, D.  
727 A. (2002). Crystal structure of aurora-2, an oncogenic serine/threonine kinase. *J Biol  
728 Chem*, 277(45), 42419-42422. doi:10.1074/jbc.C200426200
- 729 Chen, C., Ha, B. H., Thevenin, A. F., Lou, H. J., Zhang, R., Yip, K. Y., . . . Turk, B. E. (2014).  
730 Identification of a major determinant for serine-threonine kinase phosphoacceptor  
731 specificity. *Molecular Cell*, 53(1), 140-147. doi:10.1016/j.molcel.2013.11.013
- 732 Chen, V. B., Arendall, W. B., 3rd, Headd, J. J., Keedy, D. A., Immormino, R. M., Kapral, G. J., . . .  
733 Richardson, D. C. (2010). MolProbity: all-atom structure validation for  
734 macromolecular crystallography. *Acta Crystallogr D Biol Crystallogr*, 66(Pt 1), 12-21.  
735 doi:10.1107/S09074444909042073
- 736 Cohen, P. (2002). Protein kinases - the major drug targets of the twenty-first century? *Nature  
737 Reviews Drug Discovery*, 1(4), 309-315. doi:10.1038/nrd773
- 738 Copeland, R. A. (2016). The drug-target residence time model: a 10-year retrospective.  
739 *Nature Reviews Drug Discovery*, 15(2), 87-95. doi:10.1038/nrd.2015.18
- 740 Copeland, R. A., Pompliano, D. L., & Meek, T. D. (2006). Drug-target residence time and its  
741 implications for lead optimization. *Nature Reviews Drug Discovery*, 5(9), 730-739.  
742 doi:10.1038/nrd2082
- 743 Crowley, P. B., Kyne, C., & Monteith, W. B. (2012). Simple and inexpensive incorporation of  
744 <sup>19</sup>F-tryptophan for protein NMR spectroscopy. *Chem Commun (Camb)*, 48(86),  
745 10681-10683. doi:10.1039/c2cc35347d

- 746 Delaglio, F., Grzesiek, S., Vuister, G. W., Zhu, G., Pfeifer, J., & Bax, A. (1995). NMRPipe: a  
747 multidimensional spectral processing system based on UNIX pipes. *J Biomol NMR*,  
748 6(3), 277-293.
- 749 DiMaio, F., Echols, N., Headd, J. J., Terwilliger, T. C., Adams, P. D., & Baker, D. (2013). Improved  
750 low-resolution crystallographic refinement with Phenix and Rosetta. *Nat Methods*,  
751 10(11), 1102-1104. doi:10.1038/nmeth.2648
- 752 Dodson, C. A., Kosmopoulou, M., Richards, M. W., Atrash, B., Bavetsias, V., Blagg, J., & Bayliss,  
753 R. (2010). Crystal structure of an Aurora-A mutant that mimics Aurora-B bound to  
754 MLN8054: insights into selectivity and drug design. *Biochemical Journal*, 427, 19-28.  
755 doi:10.1042/Bj20091530
- 756 Emsley, P., & Cowtan, K. (2004). Coot: model-building tools for molecular graphics. *Acta*  
757 *Crystallogr D Biol Crystallogr*, 60(Pt 12 Pt 1), 2126-2132.  
758 doi:10.1107/S0907444904019158
- 759 Emsley, P., Lohkamp, B., Scott, W. G., & Cowtan, K. (2010). Features and development of Coot.  
760 *Acta Crystallogr D Biol Crystallogr*, 66(Pt 4), 486-501.  
761 doi:10.1107/S0907444910007493
- 762 Evans, P. R., & Murshudov, G. N. (2013). How good are my data and what is the resolution?  
763 *Acta Crystallogr D Biol Crystallogr*, 69(Pt 7), 1204-1214.  
764 doi:10.1107/S0907444913000061
- 765 Fancelli, D., Moll, J., Varasi, M., Bravo, R., Artico, R., Berta, D., . . . Vianello, P. (2006). 1,4,5,6-  
766 tetrahydropyrrolo[3,4-c]pyrazoles: identification of a potent Aurora kinase inhibitor  
767 with a favorable antitumor kinase inhibition profile. *J Med Chem*, 49(24), 7247-7251.  
768 doi:10.1021/jm060897w
- 769 Ferguson, F. M., Doctor, Z. M., Chaikuad, A., Sim, T., Kim, N. D., Knapp, S., & Gray, N. S. (2017).  
770 Characterization of a highly selective inhibitor of the Aurora kinases. *Bioorg Med*  
771 *Chem Lett*, 27(18), 4405-4408. doi:10.1016/j.bmcl.2017.08.016
- 772 Fraedrich, K., Schrader, J., Ittrich, H., Keller, G., Gontarewicz, A., Matzat, V., . . . Benten, D.  
773 (2012). Targeting Aurora Kinases with Danusertib (PHA-739358) Inhibits Growth of  
774 Liver Metastases from Gastroenteropancreatic Neuroendocrine Tumors in an  
775 Orthotopic Xenograft Model. *Clinical Cancer Research*, 18(17), 4621-4632.  
776 doi:10.1158/1078-0432.Ccr-11-2968
- 777 Fu, J. Y., Bian, M. L., Jiang, Q., & Zhang, C. M. (2007). Roles of aurora kinases in mitosis and  
778 tumorigenesis. *Molecular Cancer Research*, 5(1), 1-10. doi:10.1158/1541-7786.Mcr-  
779 06-0208
- 780 Gautschi, O., Heighway, J., Mack, P. C., Purnell, P. R., Lara, P. N., & Gandara, D. R. (2008). Aurora  
781 kinases as anticancer drug targets. *Clinical Cancer Research*, 14(6), 1639-1648.  
782 doi:10.1158/1078-0432.Ccr-07-2179
- 783 Gilbert, J. A. H., Sarkar, H., Sheldrake, P., Blagg, J., Ying, L., & Dodson, C. A. (2017). Dynamic  
784 Equilibrium of the Aurora A Kinase Activation Loop Revealed by Single-Molecule  
785 Spectroscopy. *Angew Chem Int Ed Engl*, 56(38), 11409-11414.  
786 doi:10.1002/anie.201704654
- 787 Goddard, T. D. K., D.G. (2008). SPARKY 3 (Version 3.115). San Francisco: University of  
788 California.
- 789 Helmus, J. J., & Jaroniec, C. P. (2013). NmrGlue: an open source Python package for the  
790 analysis of multidimensional NMR data. *J Biomol NMR*, 55(4), 355-367.  
791 doi:10.1007/s10858-013-9718-x



- 792 Heron, N. M., Anderson, M., Blowers, D. P., Breed, J., Eden, J. M., Green, S., . . . Rowsell, S. (2006).  
793 SAR and inhibitor complex structure determination of a novel class of potent and  
794 specific Aurora kinase inhibitors. *Bioorg Med Chem Lett*, 16(5), 1320-1323.  
795 doi:10.1016/j.bmcl.2005.11.053
- 796 Hopkins, A. L., & Groom, C. R. (2002). The druggable genome. *Nature Reviews Drug Discovery*,  
797 1(9), 727-730. doi:10.1038/nrd892
- 798 Howard, S., Berdini, V., Boulstridge, J. A., Carr, M. G., Cross, D. M., Curry, J., . . . Wyatt, P. G.  
799 (2009). Fragment-based discovery of the pyrazol-4-yl urea (AT9283), a multitargeted  
800 kinase inhibitor with potent aurora kinase activity. *J Med Chem*, 52(2), 379-388.  
801 doi:10.1021/jm800984v
- 802 Iqbal, N., & Iqbal, N. (2014). Imatinib: a breakthrough of targeted therapy in cancer.  
803 *Chemother Res Pract*, 2014, 357027. doi:10.1155/2014/357027
- 804 Janecek, M., Rossmann, M., Sharma, P., Emery, A., Huggins, D. J., Stockwell, S. R., . . .  
805 Venkitaraman, A. R. (2016). Allosteric modulation of AURKA kinase activity by a  
806 small-molecule inhibitor of its protein-protein interaction with TPX2. *Sci Rep*, 6,  
807 28528. doi:10.1038/srep28528
- 808 Johnson, K. A. (2009). Fitting enzyme kinetic data with KinTek Global Kinetic Explorer.  
809 *Methods Enzymol*, 467, 601-626. doi:10.1016/S0076-6879(09)67023-3
- 810 Johnson, K. A., Simpson, Z. B., & Blom, T. (2009). Global Kinetic Explorer: A new computer  
811 program for dynamic simulation and fitting of kinetic data. *Analytical Biochemistry*,  
812 387(1), 20-29. doi:10.1016/j.ab.2008.12.024
- 813 Kabsch, W. (2010). Xds. *Acta Crystallogr D Biol Crystallogr*, 66(Pt 2), 125-132.  
814 doi:10.1107/S0907444909047337
- 815 Katayama, H., & Sen, S. (2010). Aurora kinase inhibitors as anticancer molecules. *Biochimica*  
816 *Et Biophysica Acta-Gene Regulatory Mechanisms*, 1799(10-12), 829-839.  
817 doi:10.1016/j.bbagr.2010.09.004
- 818 Kilchmann, F., Marcaida, M. J., Kotak, S., Schick, T., Boss, S. D., Awale, M., . . . Reymond, J. L.  
819 (2016). Discovery of a Selective Aurora A Kinase Inhibitor by Virtual Screening. *J Med*  
820 *Chem*, 59(15), 7188-7211. doi:10.1021/acs.jmedchem.6b00709
- 821 Kitevski-LeBlanc, J. L., & Prosser, R. S. (2012). Current applications of 19F NMR to studies of  
822 protein structure and dynamics. *Prog Nucl Magn Reson Spectrosc*, 62, 1-33.  
823 doi:10.1016/j.pnmrs.2011.06.003
- 824 Kollareddy, M., Zheleva, D., Dzubak, P., Brahmshatriya, P. S., Lepsik, M., & Hajduch, M.  
825 (2012). Aurora kinase inhibitors: progress towards the clinic. *Invest New Drugs*,  
826 30(6), 2411-2432. doi:10.1007/s10637-012-9798-6
- 827 Kornev, A. P., & Taylor, S. S. (2010). Defining the conserved internal architecture of a protein  
828 kinase. *Biochimica Et Biophysica Acta-Proteins and Proteomics*, 1804(3), 440-444.  
829 doi:10.1016/j.bbapap.2009.10.017
- 830 Kornev, A. P., & Taylor, S. S. (2015). Dynamics-Driven Allostery in Protein Kinases. *Trends*  
831 *Biochem Sci*, 40(11), 628-647. doi:10.1016/j.tibs.2015.09.002
- 832 Kowiel, M., Jaskolski, M., & Dauter, Z. (2014). ACHESYM: an algorithm and server for  
833 standardized placement of macromolecular models in the unit cell. *Acta Crystallogr D*  
834 *Biol Crystallogr*, 70(Pt 12), 3290-3298. doi:10.1107/S1399004714024572
- 835 Langer, T., Vogtherr, M., Elshorst, B., Betz, M., Schieberr, U., Saxena, K., & Schwalbe, H. (2004).  
836 NMR backbone assignment of a protein kinase catalytic domain by a combination of

- 837 several approaches: application to the catalytic subunit of cAMP-dependent protein  
838 kinase. *Chembiochem*, 5(11), 1508-1516. doi:10.1002/cbic.200400129
- 839 Lemaire, P. A., Tessmer, I., Craig, R., Erie, D. A., & Cole, J. L. (2006). Unactivated PKR exists in  
840 an open conformation capable of binding nucleotides. *Biochemistry*, 45(30), 9074-  
841 9084. doi:10.1021/bi060567d
- 842 Liu, Y., & Gray, N. S. (2006). Rational design of inhibitors that bind to inactive kinase  
843 conformations. *Nat Chem Biol*, 2(7), 358-364. doi:10.1038/nchembio799
- 844 Lok, W., Klein, R. Q., & Saif, M. W. (2010). Aurora kinase inhibitors as anti-cancer therapy.  
845 *Anticancer Drugs*, 21(4), 339-350. doi:10.1097/CAD.0b013e3283350dd1
- 846 Lovera, S., Sutto, L., Boubeva, R., Scapozza, L., Dolker, N., & Gervasio, F. L. (2012). The different  
847 flexibility of c-Src and c-Abl kinases regulates the accessibility of a druggable inactive  
848 conformation. *J Am Chem Soc*, 134(5), 2496-2499. doi:10.1021/ja210751t
- 849 Lukasiwicz, K. B., & Lingle, W. L. (2009). Aurora A, centrosome structure, and the  
850 centrosome cycle. *Environ Mol Mutagen*, 50(8), 602-619. doi:10.1002/em.20533
- 851 Martin, M. P., Zhu, J. Y., Lawrence, H. R., Pireddu, R., Luo, Y., Alam, R., . . . Schonbrunn, E. (2012).  
852 A novel mechanism by which small molecule inhibitors induce the DFG flip in Aurora  
853 A. *ACS Chem Biol*, 7(4), 698-706. doi:10.1021/cb200508b
- 854 Marumoto, T., Zhang, D. W., & Saya, H. (2005). Aurora-A - A guardian of poles. *Nature Reviews*  
855 *Cancer*, 5(1), 42-50. doi:10.1038/nrc1526
- 856 Marzo, I., & Naval, J. (2013). Antimitotic drugs in cancer chemotherapy: Promises and pitfalls.  
857 *Biochemical Pharmacology*, 86(6), 703-710. doi:10.1016/j.bcp.2013.07.010
- 858 McCoy, A. J., Grosse-Kunstleve, R. W., Adams, P. D., Winn, M. D., Storoni, L. C., & Read, R. J.  
859 (2007). Phaser crystallographic software. *Journal of Applied Crystallography*, 40(Pt 4),  
860 658-674. doi:10.1107/S0021889807021206
- 861 McIntyre, P. J., Collins, P. M., Vrzal, L., Birchall, K., Arnold, L. H., Mpamhanga, C., . . . Bayliss, R.  
862 (2017). Characterization of Three Druggable Hot-Spots in the Aurora-A/TPX2  
863 Interaction Using Biochemical, Biophysical, and Fragment-Based Approaches. *ACS*  
864 *Chem Biol*, 12(11), 2906-2914. doi:10.1021/acscchembio.7b00537
- 865 Meng, Y., Lin, Y. L., & Roux, B. (2015). Computational study of the "DFG-flip" conformational  
866 transition in c-Abl and c-Src tyrosine kinases. *J Phys Chem B*, 119(4), 1443-1456.  
867 doi:10.1021/jp511792a
- 868 Nagar, B., Bornmann, W. G., Pellicena, P., Schindler, T., Veach, D. R., Miller, W. T., . . . Kuriyan,  
869 J. (2002). Crystal structures of the kinase domain of c-Abl in complex with the small  
870 molecule inhibitors PD173955 and imatinib (STI-571). *Cancer Res*, 62(15), 4236-  
871 4243.
- 872 Ni, Q., Shaffer, J., & Adams, J. A. (2000). Insights into nucleotide binding in protein kinase A  
873 using fluorescent adenosine derivatives. *Protein Sci*, 9(9), 1818-1827.  
874 doi:10.1110/ps.9.9.1818
- 875 Nikonova, A. S., Astsaturov, I., Serebriiskii, I. G., Dunbrack, R. L., Jr., & Golemis, E. A. (2013).  
876 Aurora A kinase (AURKA) in normal and pathological cell division. *Cell Mol Life Sci*,  
877 70(4), 661-687. doi:10.1007/s00018-012-1073-7
- 878 Nowakowski, J., Cronin, C. N., McRee, D. E., Knuth, M. W., Nelson, C. G., Pavletich, N. P., . . .  
879 Thompson, D. A. (2002). Structures of the cancer-related Aurora-A, FAK, and EphA2  
880 protein kinases from nanovolume crystallography. *Structure*, 10(12), 1659-1667.

- 881 Pettersen, E. F., Goddard, T. D., Huang, C. C., Couch, G. S., Greenblatt, D. M., Meng, E. C., & Ferrin,  
882 T. E. (2004). UCSF Chimera--a visualization system for exploratory research and  
883 analysis. *J Comput Chem*, 25(13), 1605-1612. doi:10.1002/jcc.20084
- 884 Sarvagalla, S., & Coumar, M. S. (2015). Structural Biology Insight for the Design of Sub-type  
885 Selective Aurora Kinase Inhibitors. *Curr Cancer Drug Targets*, 15(5), 375-393.
- 886 Schindler, T., Bornmann, W., Pellicena, P., Miller, W. T., Clarkson, B., & Kuriyan, J. (2000).  
887 Structural mechanism for STI-571 inhibition of abelson tyrosine kinase. *Science*,  
888 289(5486), 1938-1942.
- 889 Seeliger, M. A., Nagar, B., Frank, F., Cao, X., Henderson, M. N., & Kuriyan, J. (2007). c-Src binds  
890 to the cancer drug imatinib with an inactive Abl/c-Kit conformation and a distributed  
891 thermodynamic penalty. *Structure*, 15(3), 299-311. doi:10.1016/j.str.2007.01.015
- 892 Steeghs, N., Eskens, F. A. L. M., Gelderblom, H., Verweij, J., Nortier, J. W. R., Ouwerkerk, J., . . .  
893 de Jonge, M. J. A. (2009). Phase I Pharmacokinetic and Pharmacodynamic Study of the  
894 Aurora Kinase Inhibitor Danusertib in Patients With Advanced or Metastatic Solid  
895 Tumors. *Journal of Clinical Oncology*, 27(30), 5094-5101.  
896 doi:10.1200/Jco.2008.21.6655
- 897 Taylor, S. S., Keshwani, M. M., Steichen, J. M., & Kornev, A. P. (2012). Evolution of the  
898 eukaryotic protein kinases as dynamic molecular switches. *Philosophical  
899 Transactions of the Royal Society B-Biological Sciences*, 367(1602), 2517-2528.  
900 doi:10.1098/rstb.2012.0054
- 901 Treiber, D. K., & Shah, N. P. (2013). Ins and outs of kinase DFG motifs. *Chem Biol*, 20(6), 745-  
902 746. doi:10.1016/j.chembiol.2013.06.001
- 903 Vajpai, N., Strauss, A., Fendrich, G., Cowan-Jacob, S. W., Manley, P. W., Grzesiek, S., & Jahnke,  
904 W. (2008). Solution conformations and dynamics of ABL kinase-inhibitor complexes  
905 determined by NMR substantiate the different binding modes of imatinib/nilotinib  
906 and dasatinib. *J Biol Chem*, 283(26), 18292-18302. doi:10.1074/jbc.M801337200
- 907 Vogtherr, M., Saxena, K., Hoelder, S., Grimme, S., Betz, M., Schieberr, U., . . . Schwalbe, H.  
908 (2006). NMR characterization of kinase p38 dynamics in free and ligand-bound  
909 forms. *Angew Chem Int Ed Engl*, 45(6), 993-997. doi:10.1002/anie.200502770
- 910 Willemsen-Seegers, N., Uitdehaag, J. C., Prinsen, M. B., de Vetter, J. R., de Man, J., Sawa, M., . . .  
911 Zaman, G. J. (2017). Compound Selectivity and Target Residence Time of Kinase  
912 Inhibitors Studied with Surface Plasmon Resonance. *J Mol Biol*, 429(4), 574-586.  
913 doi:10.1016/j.jmb.2016.12.019
- 914 Wilson, C., Agafonov, R. V., Hoemberger, M., Kutter, S., Zorba, A., Halpin, J., . . . Kern, D. (2015).  
915 Kinase dynamics. Using ancient protein kinases to unravel a modern cancer drug's  
916 mechanism. *Science*, 347(6224), 882-886. doi:10.1126/science.aaa1823
- 917 Winn, M. D., Ballard, C. C., Cowtan, K. D., Dodson, E. J., Emsley, P., Evans, P. R., . . . Wilson, K. S.  
918 (2011). Overview of the CCP4 suite and current developments. *Acta Crystallogr D Biol  
919 Crystallogr*, 67(Pt 4), 235-242. doi:10.1107/S09074444910045749
- 920 Winter, G. (2010). xia2: an expert system for macromolecular crystallography data  
921 reduction. *Journal of Applied Crystallography*, 43, 186-190.  
922 doi:10.1107/S0021889809045701
- 923 Wojcik, J., Hantschel, O., Grebien, F., Kaupe, I., Bennett, K. L., Barkinge, J., . . . Koide, S. (2010).  
924 A potent and highly specific FN3 monobody inhibitor of the Abl SH2 domain. *Nat  
925 Struct Mol Biol*, 17(4), 519-527. doi:10.1038/nsmb.1793



- 926 Zhao, B., Smallwood, A., Yang, J., Koretke, K., Nurse, K., Calamari, A., . . . Lai, Z. (2008).  
927 Modulation of kinase-inhibitor interactions by auxiliary protein binding:  
928 crystallography studies on Aurora A interactions with VX-680 and with TPX2. *Protein*  
929 *Sci*, 17(10), 1791-1797. doi:10.1110/ps.036590.108
- 930 Zheng, H., Cooper, D. R., Porebski, P. J., Shabalin, I. G., Handing, K. B., & Minor, W. (2017).  
931 CheckMyMetal: a macromolecular metal-binding validation tool. *Acta Crystallogr D*  
932 *Struct Biol*, 73(Pt 3), 223-233. doi:10.1107/S2059798317001061
- 933 Zorba, A., Buosi, V., Kutter, S., Kern, N., Pontiggia, F., Cho, Y. J., & Kern, D. (2014). Molecular  
934 mechanism of Aurora A kinase autophosphorylation and its allosteric activation by  
935 TPX2. *Elife*, 3, e02667. doi:10.7554/eLife.02667

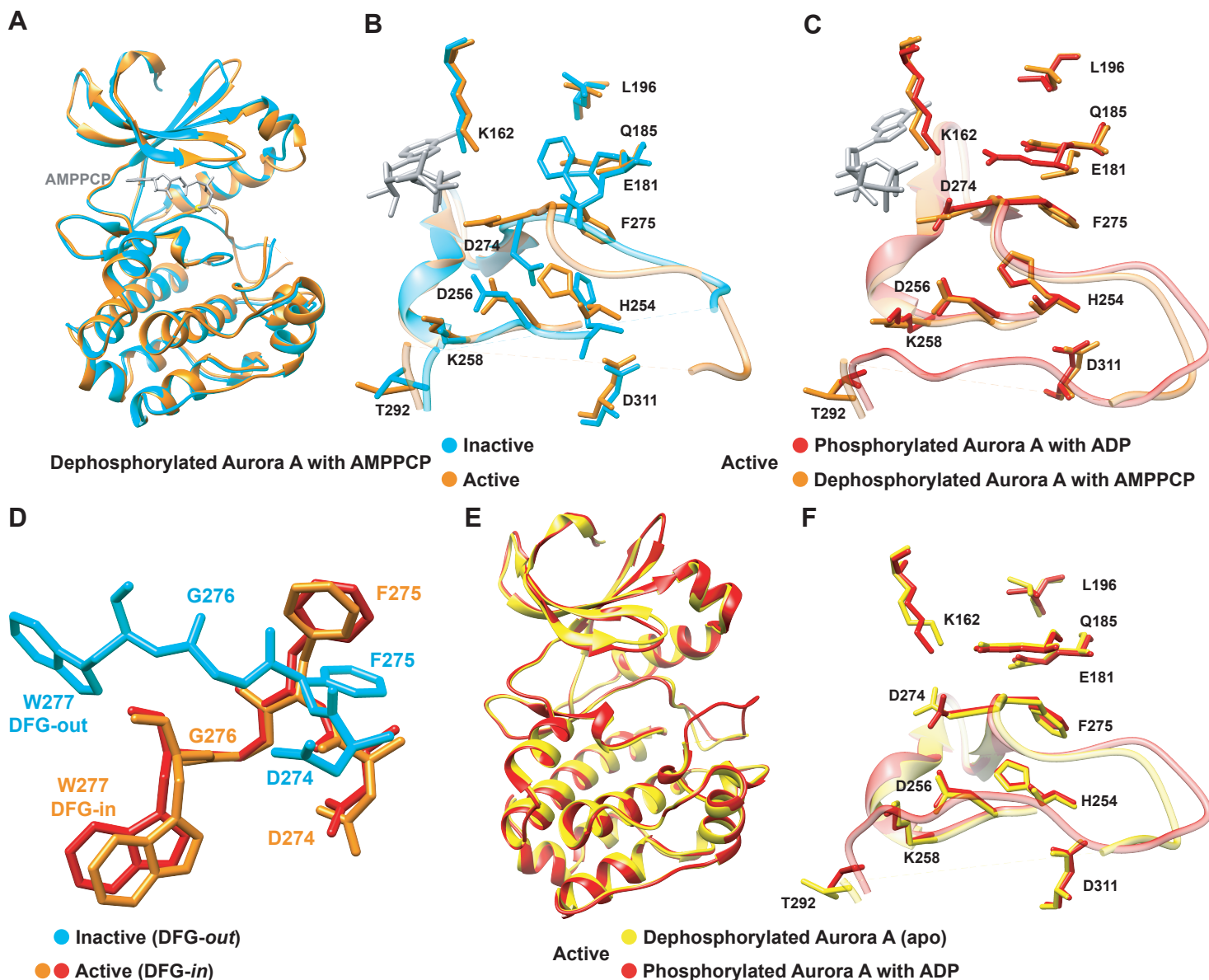


**Figure 1.** Dephosphorylated Aurora A samples both the active and inactive conformation. (A) Superposition of X-ray structures of dephosphorylated Aurora A (residues 122-403) with  $Mg^{2+}$ .AMPPCP (AMPPCP in gray sticks and magnesium as yellow sphere) in the inactive (cyan, PDB 4C3R (Zorba et al., 2014)) and active (orange, PDB 6CPF) state, solved from crystals of the same crystallization well. (B) Zoom-in of (A) to visualize the nucleotide binding region (K162, D274, and E181), the R-spine (L196, Q185, F275, H254, and D311) and the activation loop region (D256, K258, and T292). (C) Same zoom-in as in (B), but dephosphorylated Aurora A in active state (orange) is superimposed with phosphorylated Aurora A (red, PDB 1OL7 (Bayliss et al., 2003)). (D) Superposition of the DFG(W) motif in the three states shown in (B) and (C). (E) Superposition of phosphorylated Aurora A in active conformation (red) and apo, dephosphorylated Aurora A also in the active conformation (yellow, PDB 6CPE). (F) Zoom-in of (E) showing the same region as in (B).

### Data collection and refinement statistics for dephosphorylated Aurora A

	apo-Aurora A (6CPE)	Aurora A + AMPPCP (6CPF)
<b>Data collection</b>		
Space group	P 61 2 2	P 61 2 2
Cell dimensions		
<i>a, b, c</i> (Å)	80.55, 80.55, 169.79	81.75, 81.75, 172.87
$\alpha, \beta, \gamma$ (°)	90, 90, 120	90, 90, 120
Resolution (Å)	84.90 – 2.45 (2.55 – 2.45) <sup>a</sup>	86.44 – 2.30 (2.39 – 2.30) <sup>a</sup>
<i>R</i> <sub>meas</sub>	0.073 (1.308)	0.113 (2.260)
<i>I</i> / $\sigma$ ( <i>I</i> )	15.0 (1.6)	10.3 (1.3)
<i>CC</i> <sub>1/2</sub>	0.998 (0.711)	0.997 (0.465)
Completeness (%)	99.9 (100)	100 (100)
Redundancy	7.6 (6.3)	9.7 (7.8)
<b>Refinement</b>		
Resolution (Å)	64.52 – 2.45	54.79 – 2.30
No. reflections	12617 (1224)	15756 (1527)
<i>R</i> <sub>work</sub> / <i>R</i> <sub>free</sub>	0.2151 / 0.2528	0.2179 / 0.2587
No. atoms		
Protein	2035	2055
Ligand/ion	11	32
Water	4	6
<i>B</i> factors		
Protein	71.83	63.68
Ligand/ion	75.77	76.44
Water	52.52	45.84
R.m.s. deviations		
Bond lengths (Å)	0.005	0.004
Bond angles (°)	0.98	0.97

The number of crystals for each structure is 1.

<sup>a</sup> Values in parentheses are for highest-resolution shell.

**Figure 1-figure supplement 1**

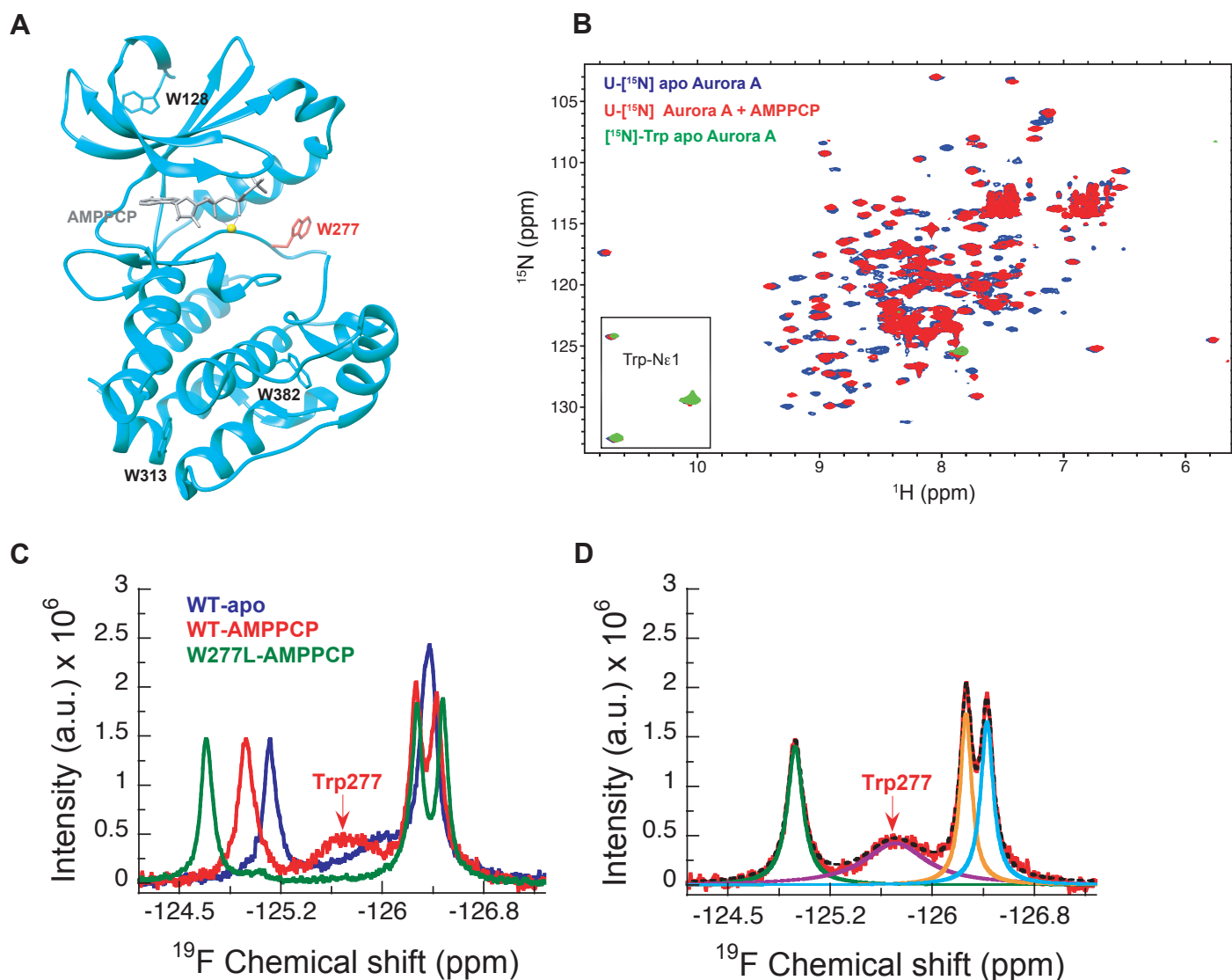


**Figure 2.** NMR spectra indicate extensive dynamics of the DFG-loop. (A) The four tryptophan residues in Aurora A are shown on the structure (PDB 4C3R (Zorba et al., 2014)) in stick representation; Trp277 in the DFGW-loop is highlighted in red. (B) Overlay of [<sup>1</sup>H-<sup>15</sup>N]-TROSY-HSQC spectra of dephosphorylated Aurora A in its apo-state (U-[<sup>15</sup>N], blue; [<sup>15</sup>N]-Trp, green) and AMPPCP-bound (U-[<sup>15</sup>N], red). Only three instead of the four expected cross peaks for tryptophan side chains are detected. (C) <sup>19</sup>F NMR spectra of 5-fluoro-Trp labeled dephosphorylated wild-type Aurora A (apo in blue and AMPPCP-bound in red) and the W277L Aurora A mutant bound to AMPPCP (green). The assignment of Trp277 following the DFG-loop is shown. (D) <sup>19</sup>F spectrum of wild-type Aurora A bound to AMPPCP (red) together with its deconvolution into four Lorentzian line shapes, the overall fit is shown as a black, dotted line. The integrals for all four signals are equal, but the linewidth for Trp277 (purple) is approximately 5-fold larger.

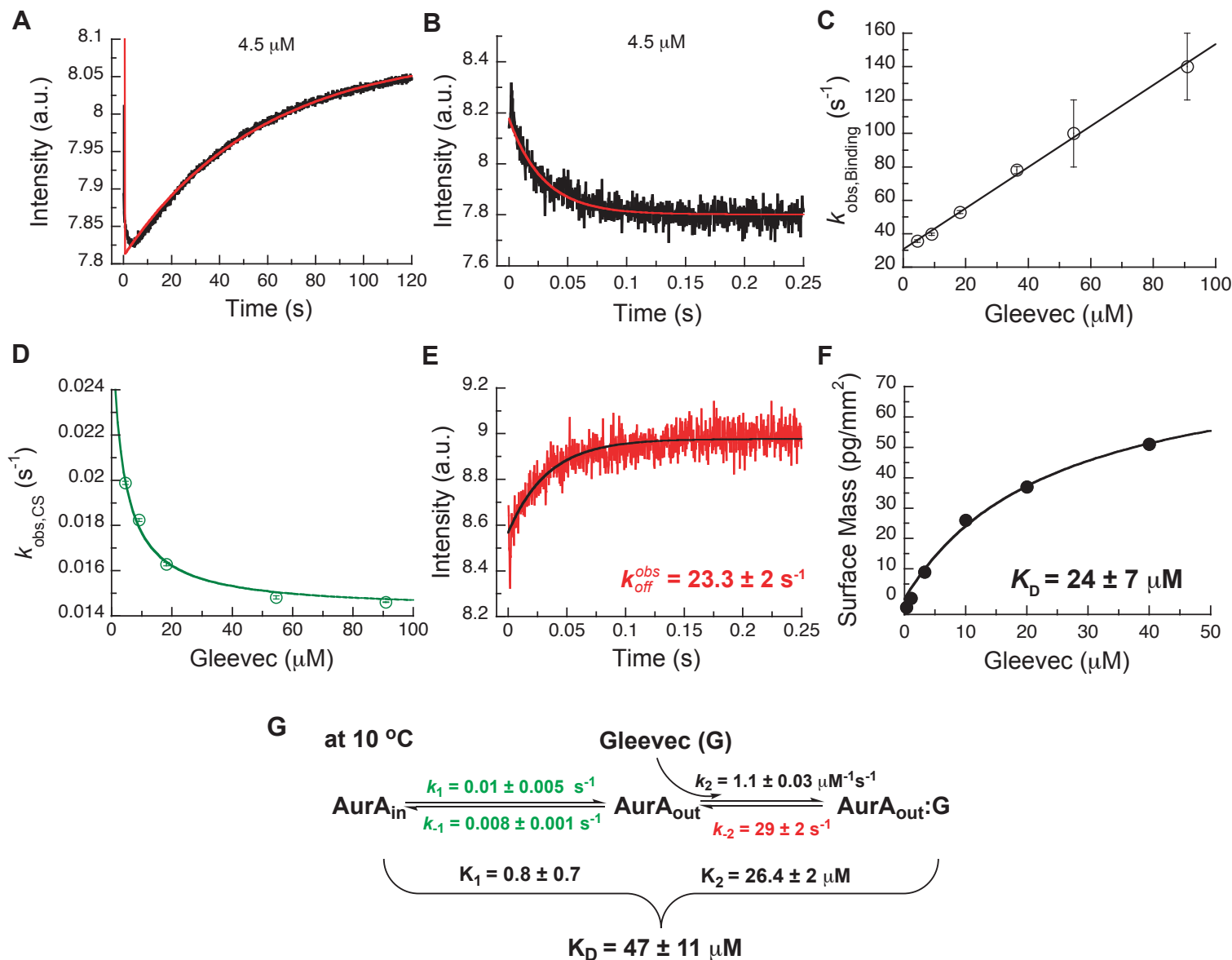


**Figure 3.** Kinetics of Gleevec binding to Aurora A at 10  $^\circ\text{C}$  measured by stopped-flow Trp fluorescence to dissect all binding steps. (A) Kinetics after mixing 0.5  $\mu\text{M}$  Aurora A with 4.5  $\mu\text{M}$  Gleevec is double exponential with a fast decrease and a slow increase in fluorescence signal. (B) The decrease in fluorescence intensity due to the fast binding phase was completed within 0.25 s. (C) Observed rate constants of fast binding phase were plotted against increasing concentrations of Gleevec ( $k_{\text{obs, Binding}} = 1.1 \pm 0.3 \mu\text{M}^{-1}\text{s}^{-1}$ ,  $k_{\text{diss}} = 31 \pm 2 \text{ s}^{-1}$  from the y-intercept). (D) The increase in fluorescence intensity of slow phase (A) is attributed to conformational selection. The plot of  $k_{\text{obs, CS}}$  of this slow phase versus Gleevec concentration was fit to Equation 1 and yields  $k_1 = 0.014 \pm 0.001 \text{ s}^{-1}$  and  $k_{-1} = 0.011 \pm 0.002 \text{ s}^{-1}$ . (E) Dissociation kinetics of pre-incubated solution with 5  $\mu\text{M}$  Aurora A and 5  $\mu\text{M}$  Gleevec measured by stopped-flow fluorescence after an 11-fold dilution of the complex yields the  $k_2 = 23.3 \pm 2 \text{ s}^{-1}$ . (F) The macroscopic dissociation constant ( $K_D$ ) of Gleevec binding to Aurora A measured by Creoptix WAVE. (G) Gleevec (labeled as G) binding scheme to Aurora A corresponds to a two-step binding mechanism: conformational selection followed by the physical binding step. The corresponding microscopic rate constants obtained from the global fit and calculated overall equilibrium and dissociation constants are shown. Fluorescence traces are the average of at least five replicate measurements ( $n > 5$ ), and error bars and uncertainties given in C-G denote the (propagated) standard deviation in the fitted parameter.

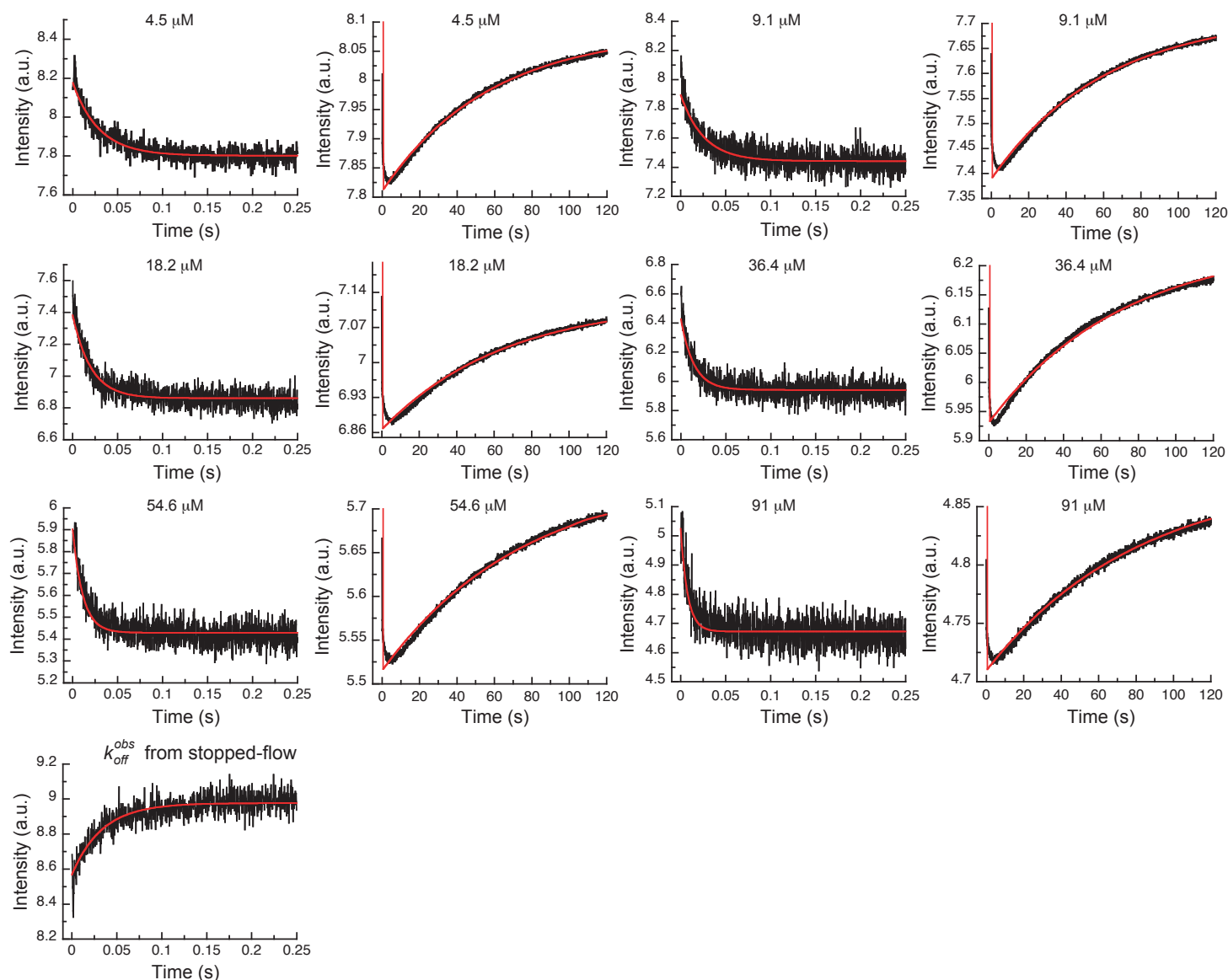


**Figure 4.** Global fits of Gleevec binding- and dissociation-kinetics to Aurora A at 10 °C. Fitting of kinetic traces (average,  $n > 5$ ) of the mixing of 0.5 μM Aurora A with different Gleevec concentrations at two timescales, 0.25 s and 120 s, and dissociation kinetics ( $k_{off}$ ) were performed using the KinTek Explorer software with the binding scheme in Figure 3G. Red lines show the results of the global fit to the experimental data in black.



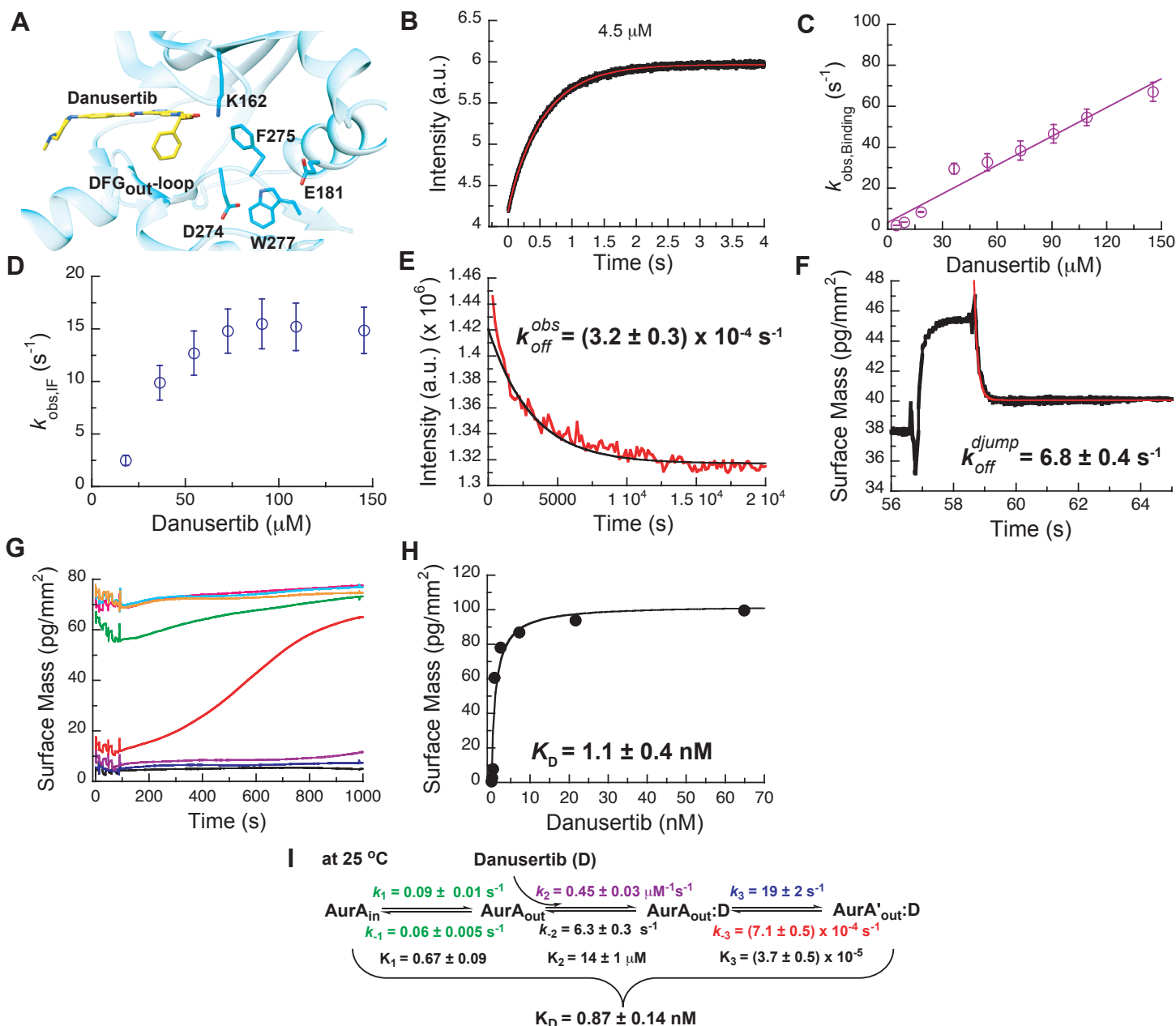


**Figure 5.** Mechanism of Danusertib binding to Aurora A at 25 °C. (A) Danusertib bound to the DFG-out conformation of Aurora A is shown highlighting important active-site residues in stick representation (PDB 2J50 (Fancelli et al., 2006)). (B) The increase in fluorescence upon Danusertib binding is fitted to a double exponential. (C) Plot of  $k_{\text{obs, Binding}}$  versus the concentration of Danusertib for the fast phase yields  $k_2 = 0.4 \pm 0.1 \mu\text{M}^{-1} \text{ s}^{-1}$  and  $k_{-2} = 4.6 \pm 3 \text{ s}^{-1}$  and the  $k_{\text{obs, IF}}$  for the slow phase (D) reaches a plateau around  $16 \pm 2 \text{ s}^{-1}$ . (E) Dissociation of Danusertib from Aurora A at 25 °C after a 30-fold dilution of the Aurora A/Danusertib complex measured by Trp-fluorescence quenching and fitting with single exponential gives a value of  $k_3 = (3.2 \pm 0.3) \times 10^{-4} \text{ s}^{-1}$ . (F) Double-jump experiment (2 s incubation time of 1  $\mu\text{M}$  Danusertib to Aurora A followed by 60 s long dissociation step initiated by a wash with buffer) was measured by Creoptix WAVE waveguide interferometry to properly define the value of  $k_{-2} = 6.8 \pm 0.4 \text{ s}^{-1}$ . (G) Macroscopic dissociation constant ( $K_{\text{D}}$ ) determined by Creoptix WAVE waveguide interferometry: surface-immobilized Aurora A was incubated with various concentrations of Danusertib (0.1 nM (black), 0.2 nM (blue), 0.4 nM (purple), 0.8 nM (red), 2.4 nM (green), 7.2 nM (pink), 21.6 nM (cyan), and 64.8 nM (orange)) and surface mass accumulation was observed until establishment of equilibrium. (H) A plot of the final equilibrium value versus Danusertib concentration yields a  $K_{\text{D}} = 1.1 \pm 0.4 \text{ nM}$ . (I) Binding scheme of Danusertib (labeled D) highlighting a three-step binding mechanism, containing both conformational selection and induced-fit step. Red lines in (B, F) and black line in (E) are the results from global fitting. Kinetic constants shown in I determined from global fitting (Figure 6). Fluorescence traces are the average of at least five replicate measurements ( $n > 5$ ), and error bars and uncertainties given in C-E, H, and I denote the (propagated) standard deviation in the fitted parameter.

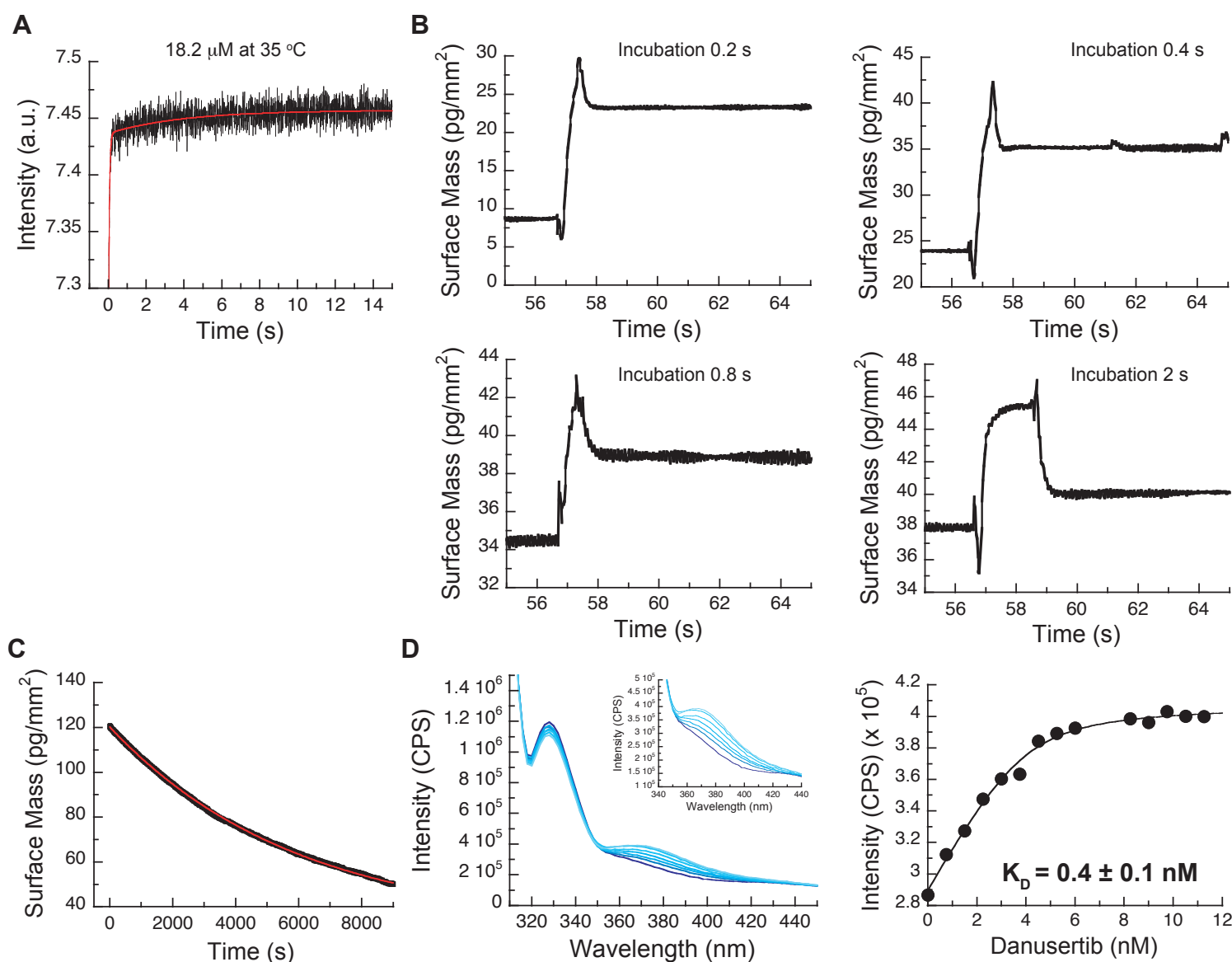


**Figure 5-figure supplement 1.** (A) Kinetic trace at 35 °C of 18.2 μM Danusertib binding to 0.1 μM Aurora A. The red line represents the best fit of the trace to a double exponential function. The initial fast increase in fluorescence is a convolution of the fast binding and induced-fit steps, whereas the slower phase gives an observed rate constant of approximately 0.1 s<sup>-1</sup>, suggestive of a third process (i.e., conformational selection). (B) Double-jump experiments measured with Creoptix WAVE waveguide interferometry at 25 °C using Danusertib and a 0.2, 0.4, 0.8 and 2 s incubation time. In the first step of the double jump, Danusertib is incubated with surface-immobilized Aurora A kinase before washing with buffer alone initiates dissociation in a second step. All traces show a single exponential decay with an observed rate constant of 6 s<sup>-1</sup> and its amplitude increases with longer incubation time as more AurA<sub>out</sub>:D is formed. (C) Dilution of the Aurora A/Danusertib complex formed after 1 hour incubation. The slow dissociation of Aurora A/Danusertib (limited by  $k_{-3}$ ) was measured by Creoptix WAVE waveguide interferometry and fitted to a single exponential with a value of  $k_{-3} = (2 \pm 0.6) \times 10^{-4}$  s<sup>-1</sup>. (D) Representative selection of emission spectra obtained after the addition of increasing concentrations of Danusertib (0 - 11.25 nM from dark to light blue) to Aurora A (excitation at 295 nm). Plot of the increase in fluorescence intensity at 368 nm versus Danusertib concentration yields a  $K_D$  value of  $0.4 \pm 0.1$  nM determined by fitting the data to Equation 6. Fluorescence trace in A is the average of five replicate measurements ( $n = 5$ ), and the uncertainties given in D denotes the standard deviation in the fitted parameter.



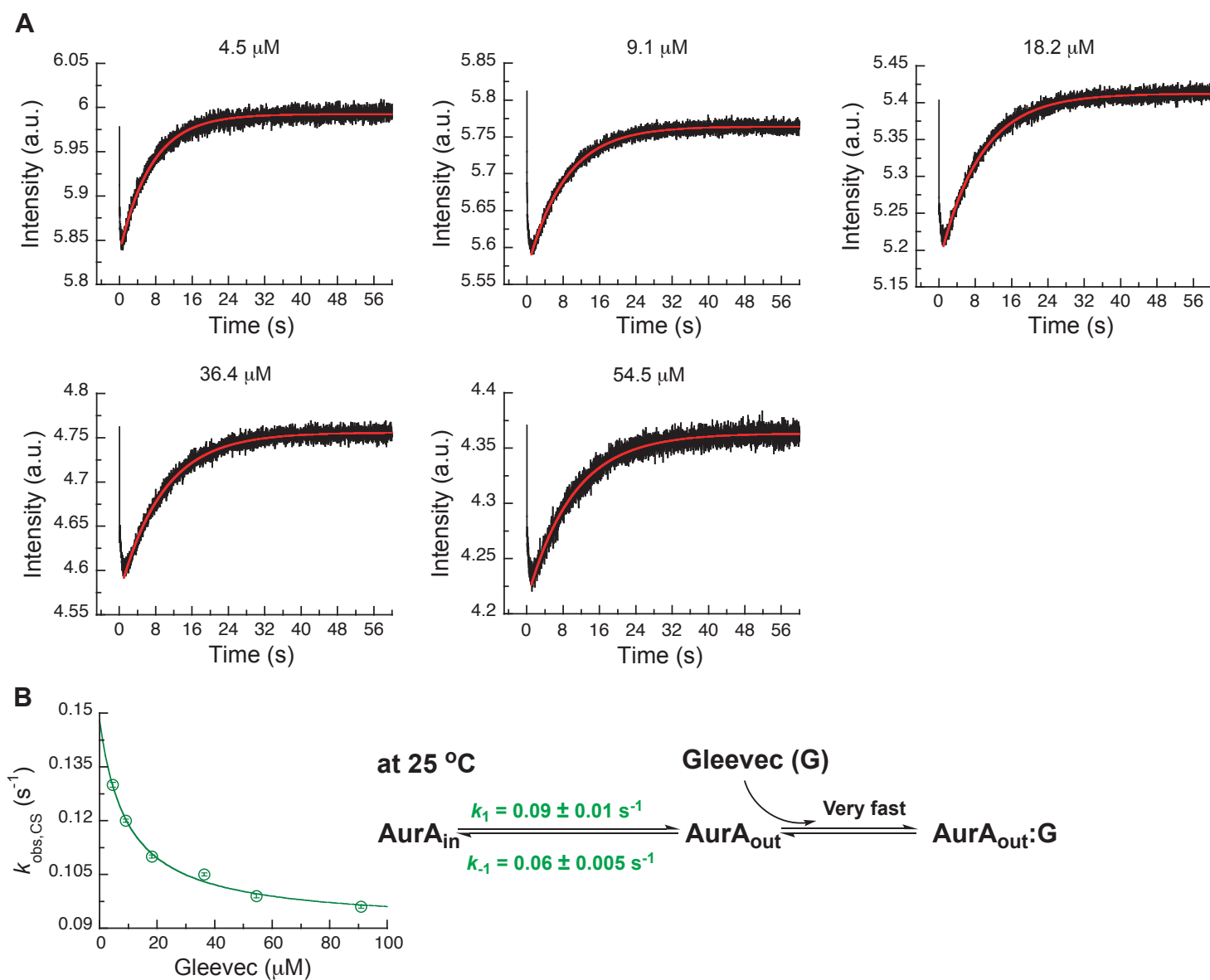


**Figure 5-figure supplement 2.** Kinetics of Gleevec binding to Aurora A at 25 °C to determine DFG-*in*/DFG-*out* equilibrium in apo Aurora A at 25 °C. (A) 0.5 μM Aurora A was mixed with shown Gleevec concentrations. The increase in fluorescence intensity of slow phase reflects the conformational selection step (see Figure 3A). (B)  $k_{\text{obs,CS}}$  of the slow phase as a function of the Gleevec concentration is an inverse hyperbolic function and fitting to Equation 1 gives  $k_1 = 0.09 \pm 0.01 \text{ s}^{-1}$  and  $k_{-1} = 0.06 \pm 0.005 \text{ s}^{-1}$ . Corresponding binding scheme is depicted. Fluorescence traces are the average of at least five replicate measurements ( $n > 5$ ), and error bars and uncertainties given in B denote the standard deviation in the fitted parameter.

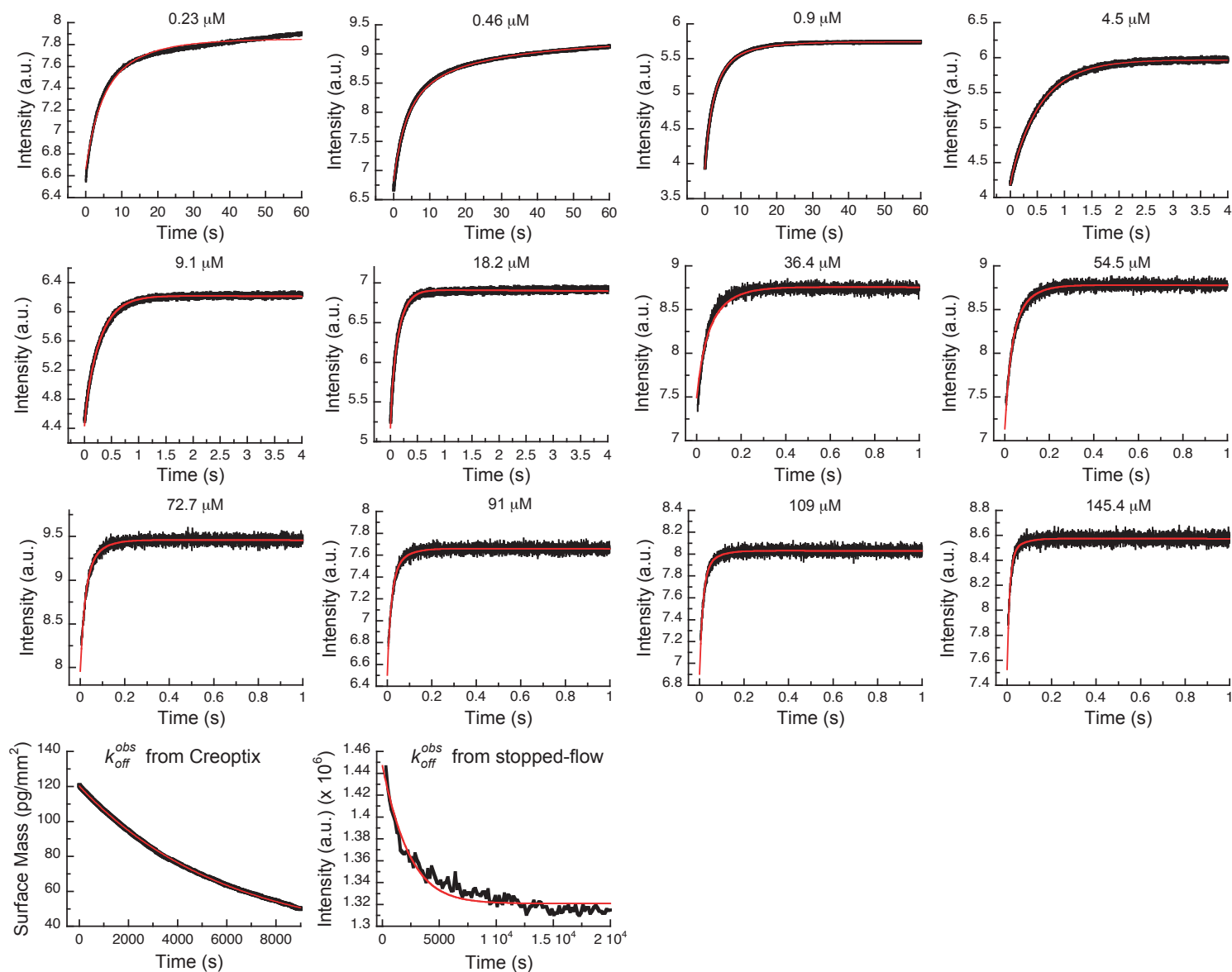
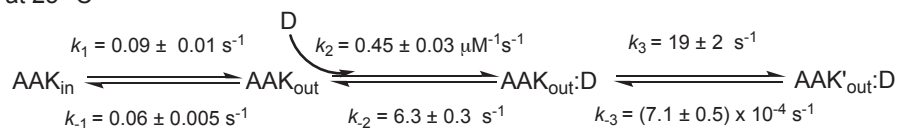


**Figure 6.** Global fits of Danusertib binding and dissociation kinetics to Aurora A at 25 °C. Binding kinetics was monitored by stopped-flow fluorescence for different concentrations of Danusertib (indicated) to 0.5 μM Aurora A, and dissociation kinetics ( $k_{obs,off}$ ) by Creoptix and fluorimeter (see Figure 5). Fluorescence traces are the average of at least five replicate measurements ( $n > 5$ ). Global fitting was performed using the KinTek Explorer software using the model shown in Figure 5I.

$$\text{Creoptix } k_{\text{slow-off}}^{\text{obs}} = (2 \pm 0.006) \times 10^{-4} \text{ s}^{-1}$$

$$\text{Fluorimeter } k_{\text{slow-off}}^{\text{obs}} = (3.2 \pm 0.3) \times 10^{-4} \text{ s}^{-1}$$

at 25 °C



Kinetic Partitioning: Aurora A with Danusertib

$$\begin{aligned}
 k_{\text{slow-off}}^{\text{obs}} &= \frac{k_{-2} \times k_{-3}}{k_{-2} + k_3 + k_{-3}} \\
 &= \frac{6.3 \times (7.1 \times 10^{-4})}{6.3 + 19 + (7.1 \times 10^{-4})}
 \end{aligned}$$

$$k_{\text{slow-off}}^{\text{obs}} = (1.77 \pm 0.2) \times 10^{-4} \text{ s}^{-1}$$

**Figure 6-figure supplement 1.** Kinetic partitioning of Aurora A with Danusertib. The apparent discrepancy between the experimentally observed off rates and the microscopic rate constant,  $k_{-3}$ , can be explained by considering the kinetic partitioning. Uncertainties given denote the (propagated) standard deviation in the fitted parameter.

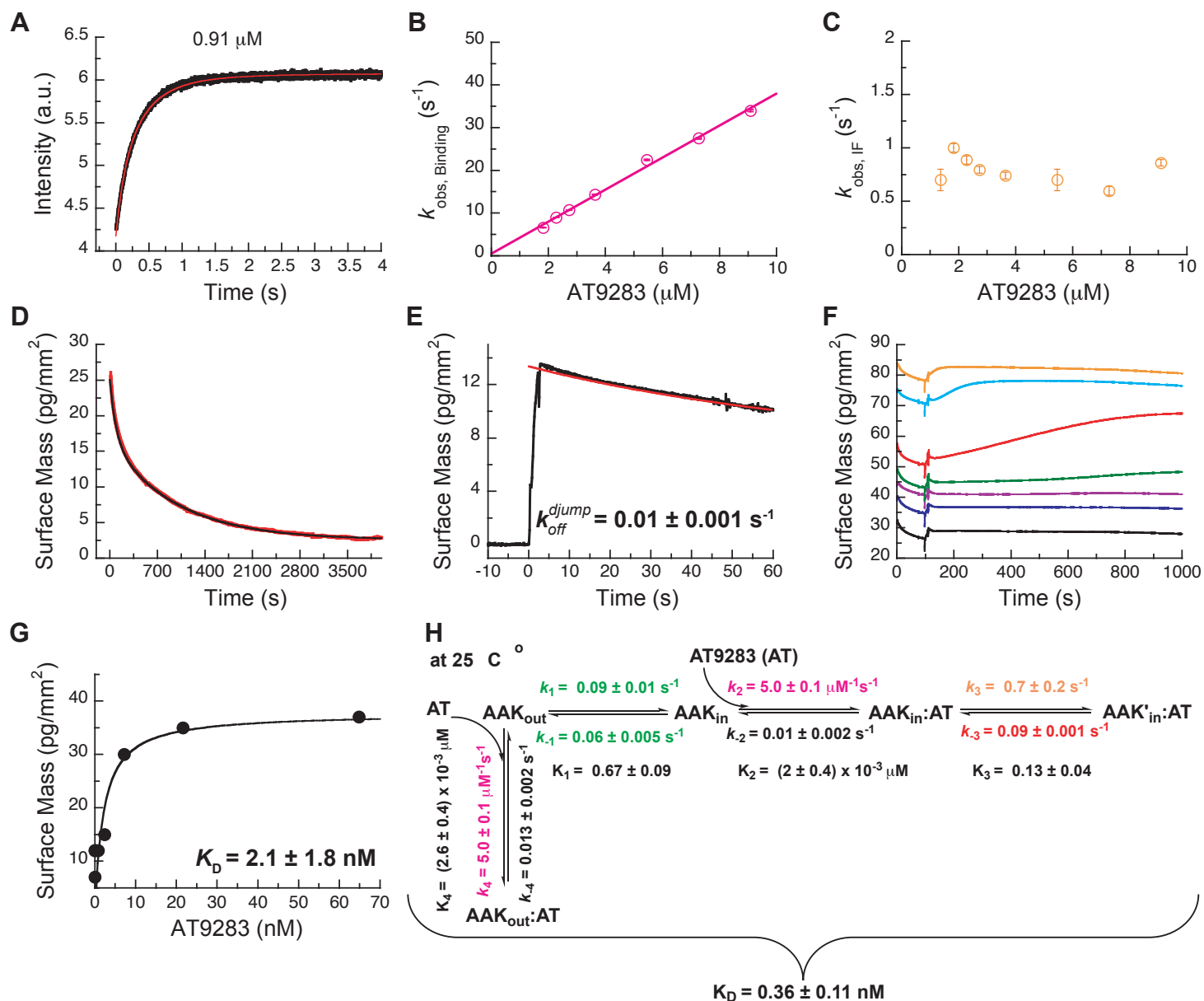


**Figure 7.** Mechanism of AT9283 drug binding to Aurora A at 25 °C. (A) The increase in fluorescence at 25 °C upon AT9283 binding fitted to a double exponential. (B) The plot of  $k_{\text{obs, Binding}}$  versus AT9283 concentration for the fast phase yields  $k_2 = 3.4 \pm 0.5 \mu\text{M}^{-1}\text{s}^{-1}$  and an underdetermined intercept ( $k_{-2}$ ) and (C) the  $k_{\text{obs}}$  of the slow phase reaches a plateau around  $0.8 \pm 0.2 \text{ s}^{-1}$ . (D) Dilution of the Aurora A/AT9283 complex formed after 1 hour incubation. The slow dissociation was measured by Creoptix WAVE waveguide interferometry and fitted with a double exponential with rate constants of  $(1.1 \pm 0.02) \times 10^{-2} \text{ s}^{-1}$  and  $(0.1 \pm 0.01) \times 10^{-2} \text{ s}^{-1}$ . (E) Double-jump experiments (1 s incubation time of 1  $\mu\text{M}$  AT9283 to Aurora A followed by 60 s long dissociation step initiated by a wash with buffer) was measured by Creoptix WAVE waveguide interferometry to properly define the value of  $k_2 = (1.0 \pm 0.1) \times 10^{-2} \text{ s}^{-1}$ . (F) Macroscopic dissociation constant ( $K_D$ ) determined by Creoptix WAVE waveguide interferometry: surface-immobilized Aurora A was incubated with various concentration of AT9283 (0.03 nM (black), 0.27 nM (blue), 0.8 nM (purple), 2.4 nM (green), 7.2 nM (red), 21.6 nM (cyan), and 64.8 nM (orange)) and surface mass accumulation was observed until establishment of equilibrium. (G) A plot of the final equilibrium value versus AT9283 concentration yields a  $K_D = 2.1 \pm 1.8 \text{ nM}$ . (H) Binding scheme for AT9283 (labeled AT) highlighting a four-steps binding mechanism, that contains binding to two different states, a conformational selection mechanism and an induced-fit step. Kinetic constants shown in H were determined from global fitting (see Figure 8). Fluorescence traces are the average of at least five replicate measurements ( $n > 5$ ), and error bars and uncertainties given in B,C,G and H denote the (propagated) standard deviation in the fitted parameter.

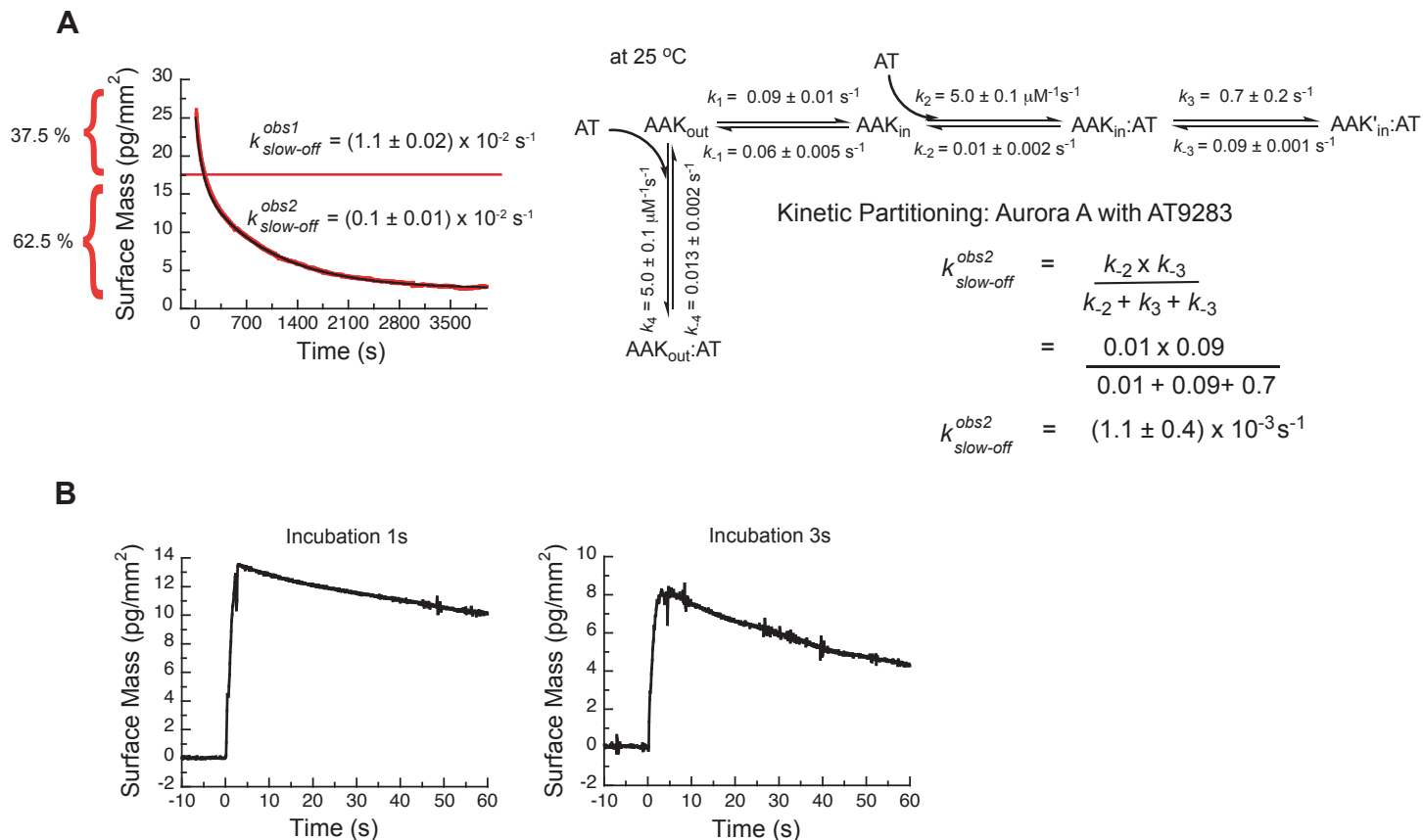


**Figure 7-figure supplement 1.** (A) Kinetic partitioning of Aurora A with AT9283. The apparent discrepancy between the experimentally observed off rates and the microscopic rate constant,  $k_3$ , can be explained by considering the kinetic partitioning. (B) Double-jump experiments measured by Creoptix WAVE waveguide interferometry at 25 °C of AT9283 at 1 and 3 s incubation time before induction of dissociation by a buffer wash are best described with a single exponential function of ( $k = 0.01 \text{ s}^{-1}$ ). Uncertainties given in A denote the (propagated) standard deviation in the fitted parameter.

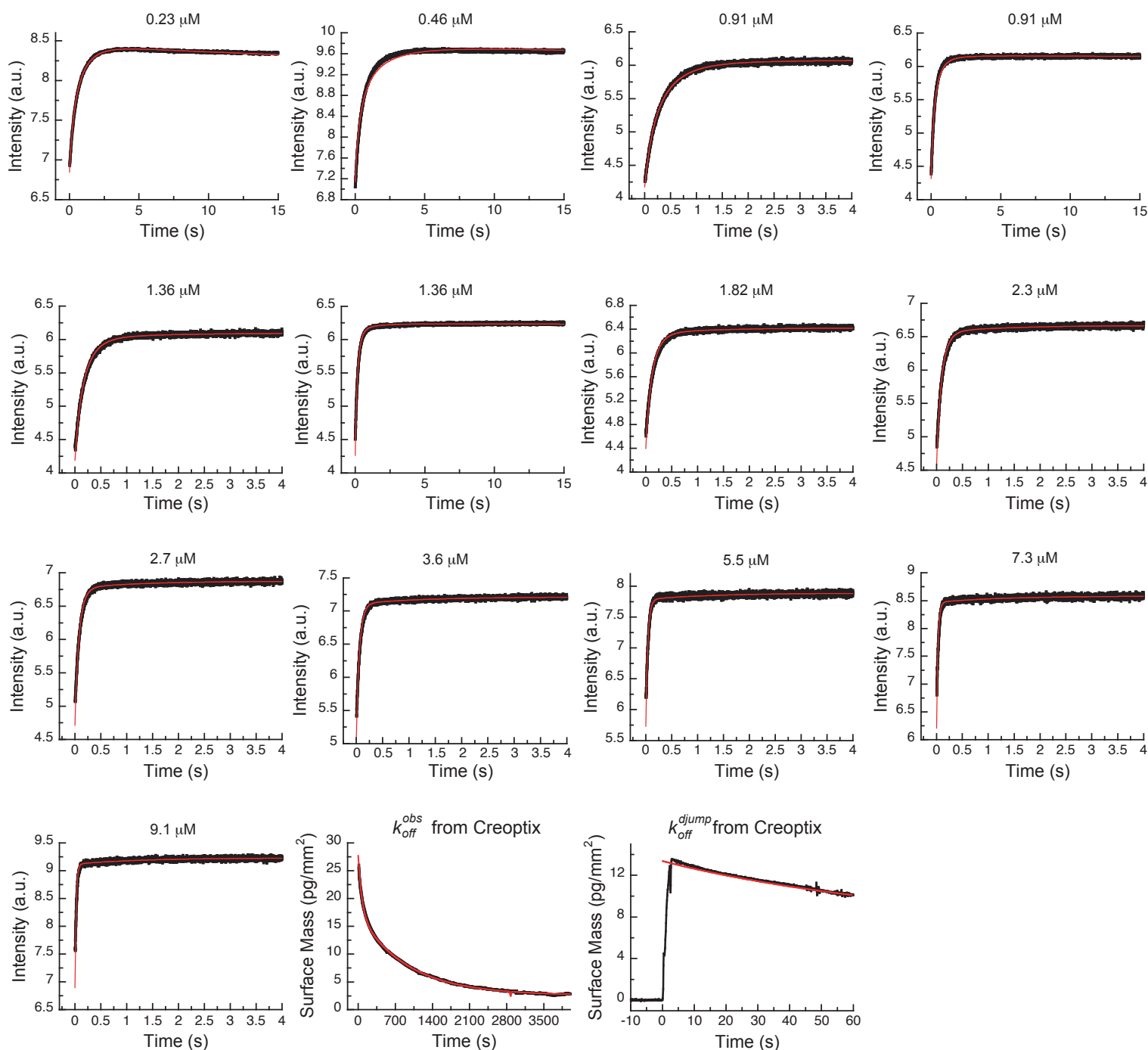


**Figure 8.** Global fits of AT9283 binding and dissociation kinetics to Aurora A at 25 °C. Binding kinetics was monitored by stopped-flow fluorescence at different concentrations of AT9283 (indicated) to 0.5 μM Aurora A. Dissociation kinetics were obtained for fully equilibrated drug/kinase complex ( $k_{\text{obs,off}}^{\text{obs}}$ ) or for the initial encounter complex ( $k_{\text{off,djump}}^{\text{djump}}$ ) by using a 1 hour or a short 2 s incubation of the kinase with AT9283, respectively, before inducing dissociation by a buffer wash using Creoptix WAVE waveguide interferometry. Global fitting was performed with KinTek Explorer software using the model in Figure 7H (reduced  $\chi^2 = 3.2$ ). Fluorescence traces are the average of at least five replicate measurements ( $n > 5$ ).

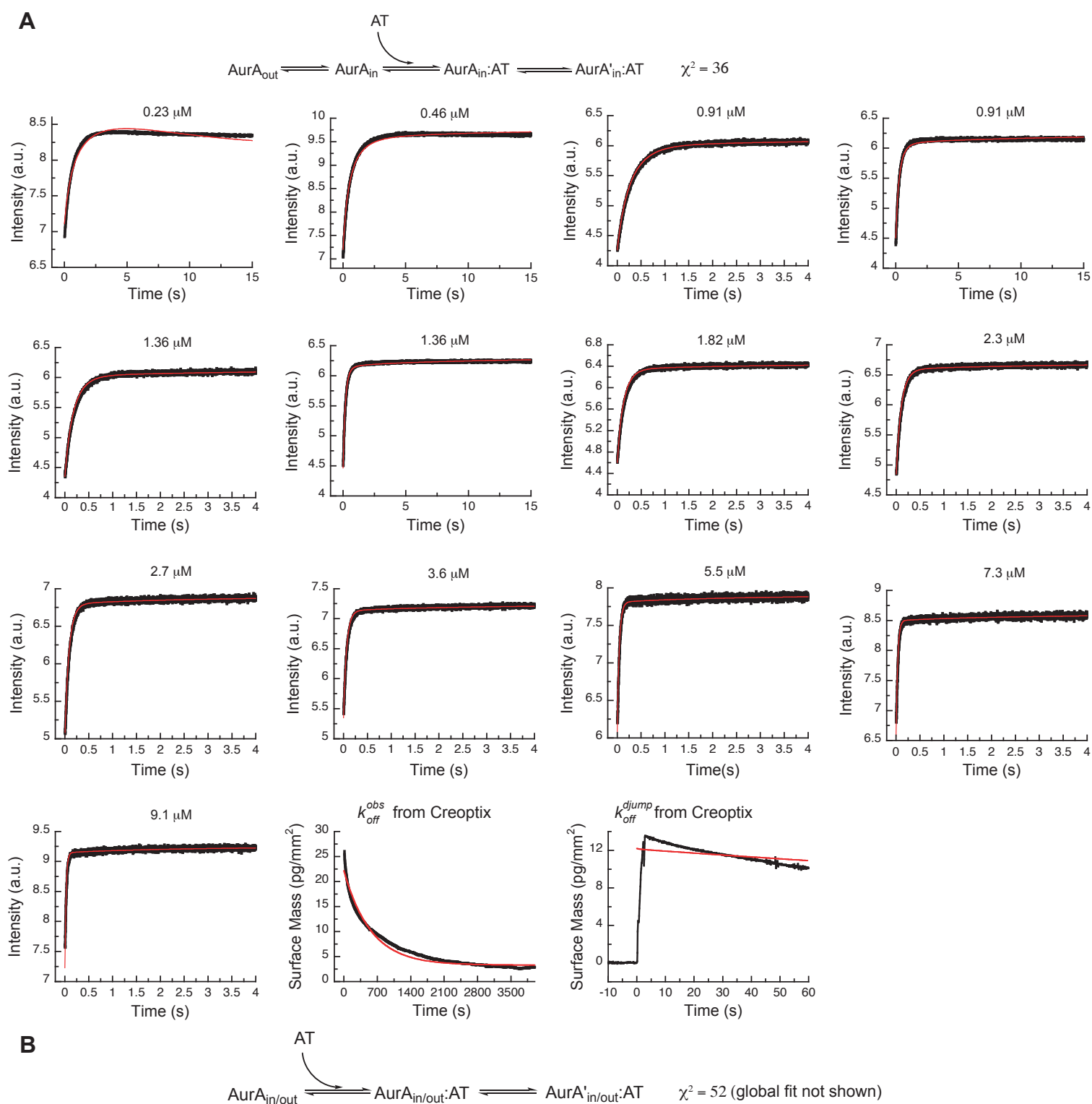


**Figure 8-figure supplement 1.** Alternative binding models of AT9283 to Aurora A cannot explain the experimental data. (A) Our initial three-state binding scheme, where AT9283 binds only the DFG<sub>in</sub> state of Aurora A and is followed by an induced-fit step, is incorrect. The best global fit (shown in red) did not describe the data as can be seen by visual inspection and from the reduced  $\chi^2$  value of 36. (B) An alternative model, where AT9283 can bind to Aurora A irrespective of the state of the DFG-loop, and binding is followed by an induced-fit step did not result in adequate fits (data not shown) and a reduced  $\chi^2$  value of 52. In both cases the values for the interconversion between  $\text{AurA}_{\text{out}}$  and  $\text{AurA}_{\text{in}}$  were taken from the Gleevec experiment (Figure 5-figure supplement 2). Fluorescence traces are the average of at least five replicate measurements ( $n > 5$ ).



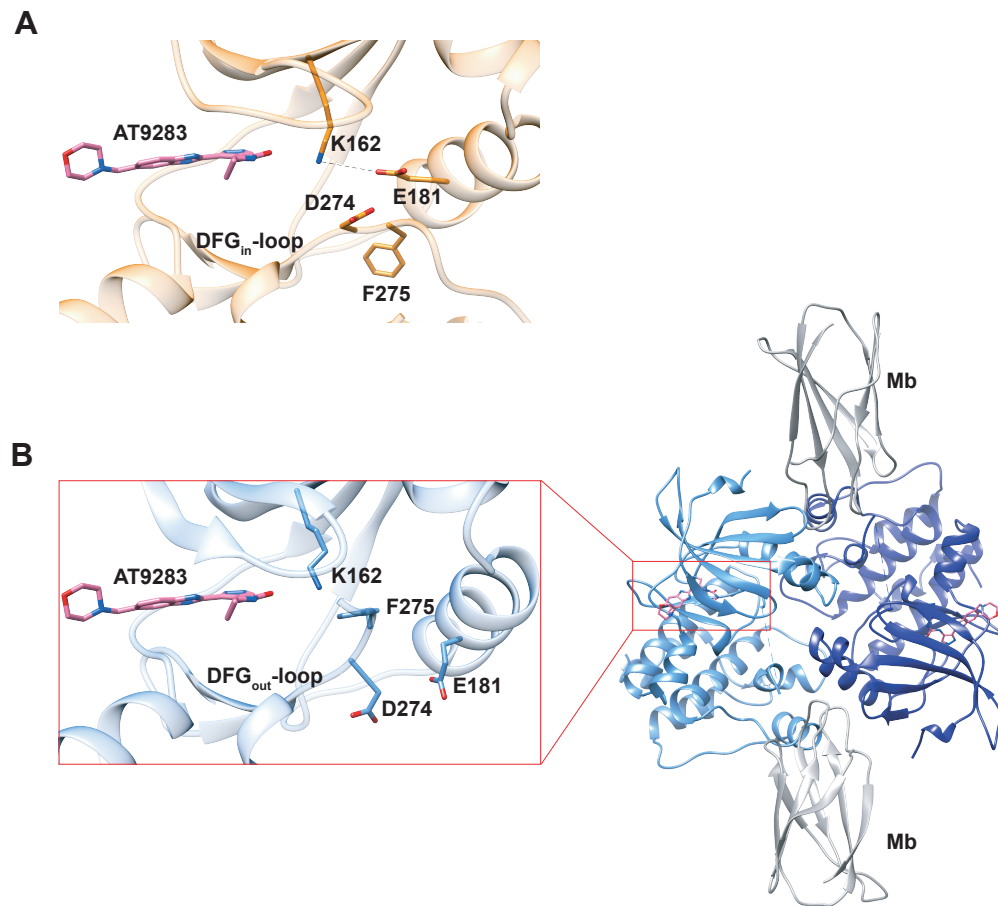


**Figure 9.** X-ray structures of Aurora A bound to inhibitor AT9283 reveal multiple binding modes. (A) AT9283 (pink) bound to the active site of Aurora A (PDB 2W1G, (Howard et al., 2009)) shows the DFG<sub>in</sub>-loop conformation and a salt bridge between K162 and E181. (B) Aurora A dimer (light and dark blue ribbon) in complex with AT9283 (pink) and inhibiting monobody (Mb, grey), showing DFG<sub>out</sub>-loop and broken K162 and E181 salt bridge (PDB 6CPG).

**Data collection and refinement statistics for dephosphorylated Aurora A in complex with monobody and AT9283**

Aurora A + Mb + AT9283 (6CPG)	
<b>Data collection</b>	
Space group	P 21 21 21
Cell dimensions	
<i>a, b, c</i> (Å)	63.86, 69.7, 175.56
$\alpha, \beta, \gamma$ (°)	90, 90, 90
Resolution (Å)	43.14 – 2.80 (2.87 – 2.80) <sup>a</sup>
<i>R</i> <sub>meas</sub>	0.189 (1.268)
<i>I</i> / $\sigma$ ( <i>I</i> )	8.9 (1.1)
<i>CC</i> <sub>1/2</sub>	0.986 (0.625)
Completeness (%)	99.2 (98.8)
Redundancy	5.4 (5.3)
<b>Refinement</b>	
Resolution (Å)	36.17 – 2.80
No. reflections	19556 (1845)
<i>R</i> <sub>work</sub> / <i>R</i> <sub>free</sub>	0.2792/ 0.3350
No. atoms	
Protein	5122
Ligand/ion	56
Water	
<i>B</i> factors	
Protein	78.84
Ligand/ion	81.05
Water	
R.m.s. deviations	
Bond lengths (Å)	0.003
Bond angles (°)	0.98

The number of crystals for each structure is 2.

<sup>a</sup> Values in parentheses are for highest-resolution shell.

**Figure 9-figure supplement 1**

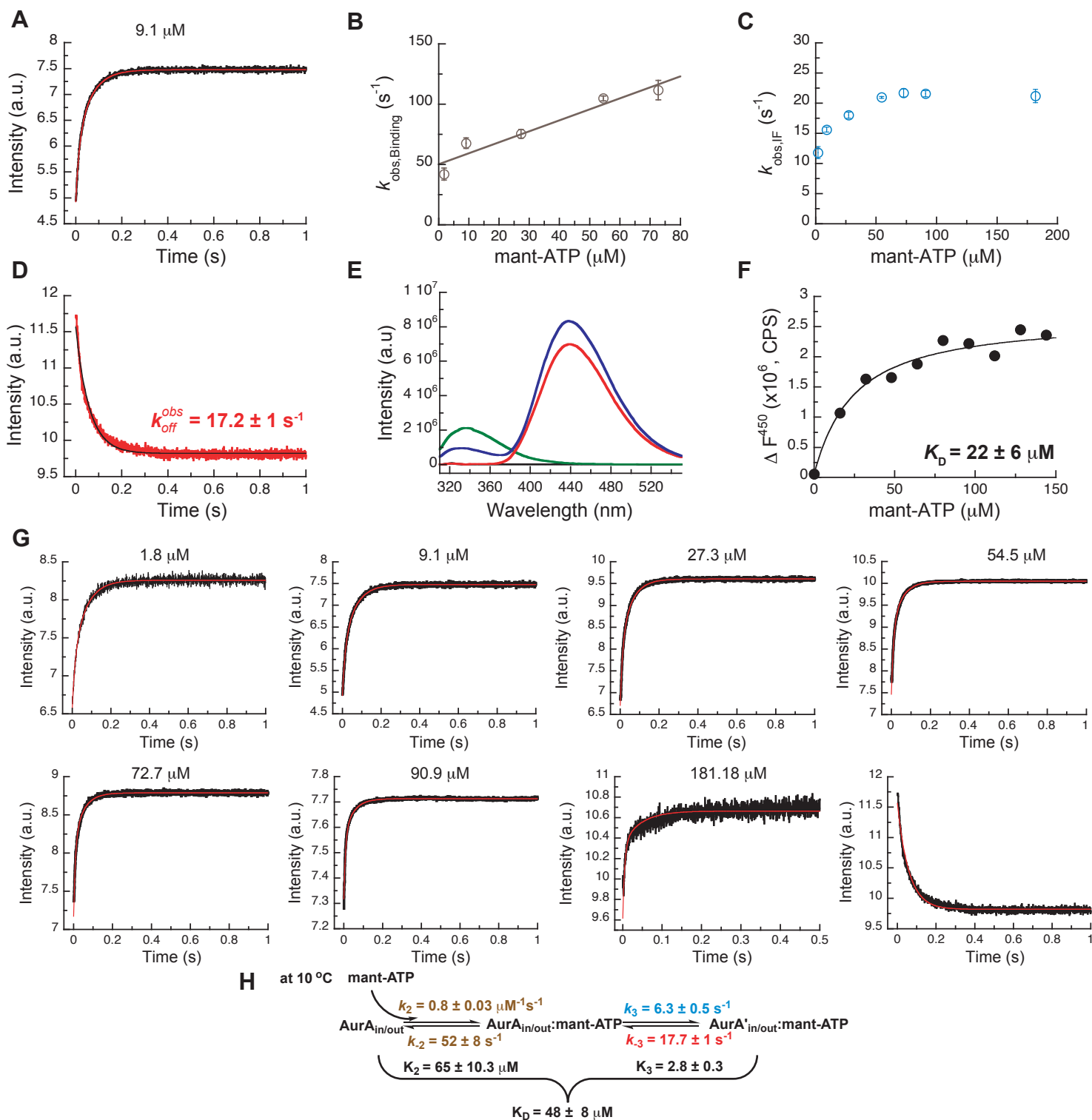


**Figure 10.** Mechanism of ATP binding to Aurora A at 10 °C. (A) Binding of mant-ATP to Aurora A was followed by an increase in fluorescence with biphasic kinetics. The plot of  $k_{\text{obs}}$  versus concentration of mant-ATP of fast phase (B) yields  $k_2 = 0.8 \pm 0.2 \mu\text{M}^{-1}\text{s}^{-1}$  and  $k_{-2} = 50 \pm 8 \text{ s}^{-1}$  and the slow phase (C) reached a plateau around  $21 \pm 1 \text{ s}^{-1}$  ( $k_3 + k_{-3}$ ). (D) Dissociation kinetics of 10  $\mu\text{M}$  Aurora A/10  $\mu\text{M}$  mant-ATP complex was measure after a 10-fold dilution into buffer and yields  $k_{\text{obs,off}} = 17.2 \pm 1 \text{ s}^{-1}$ . (E, F) Macroscopic dissociation constant of Aurora A with mant-ATP measured by fluorescence energy transfer. (E) Emission spectra (excitation at 290 nm) of 1  $\mu\text{M}$  Aurora A (green), 160  $\mu\text{M}$  mant-ATP (red), and 1  $\mu\text{M}$  Aurora A/160  $\mu\text{M}$  mant-ATP (blue). (F) The change in fluorescence at 450 nm ( $\Delta F_{450}$ ) versus mant-ATP concentrations yields  $K_D = 22 \pm 6 \mu\text{M}$ . (G) Global fitting (red) of all kinetics data (black) in KinTek Explorer to the binding scheme shown in (H) results in the kinetic constants given in the scheme and gives an overall  $K_D = 48 \pm 8 \mu\text{M}$ , calculated from all rate constants. Fluorescence traces are the average of at least five replicate measurements ( $n > 5$ ), and error bars and uncertainties given in B, C, D, F, and H denote the (propagated) standard deviation in the fitted parameter.